Hydroxyapatite: A Matrix for Metal Exsolution Leading to Highly Dispersed Catalytically Active Species

Josefine Schnee, Ferdaous Ben Romdhane, François Devred, Antoine Miche, Alixandre Magerat, Diane Reja, Eric Gaigneaux, Marco Daturi, Cyril Thomas, Guylène Costentin

Hydroxyapatite: a matrix for metal exsolution leading to highly dispersed catalytically active species

Josefine Schnee,[a,*] Ferdaous Ben Romdhane,[b] François Devred,[c] Antoine Miche,[a] Alixandre Magerat,[c] Diane Reja,[a] Eric M. Gaigneaux,[c] Marco Daturi,[d] Cyril Thomas[a,*] and Guylène Costentin[a]

[a]Sorbonne Université, CNRS, Laboratoire de Réactivité de Surface (LRS), Campus Pierre et Marie Curie, 4 Place Jussieu, F-75005 Paris, France.
[b]Fédération de Chimie et Matériaux de Paris-Centre (FCMat), Campus Pierre et Marie Curie, 4 Place Jussieu, F-75005 Paris, France.
[c]Université catholique de Louvain, Institute of Condensed Matter and Nanosciences (IMCN), Molecular Chemistry, Materials and Catalysis (MOST), Place Louis Pasteur 1 box L4.01.09, B-1348 Louvain-la-Neuve, Belgium.
[d]Normandie Université, ENSICAEN, UNICAEN, CNRS, Laboratoire Catalyse et Spectrochimie, 6 Boulevard Maréchal Juin, F-14050 Caen, France.
*Corresponding authors: josefine.schnee@sorbonne-universite.fr, cyril.thomas@sorbonne-universite.fr.

Keywords: Hydroxyapatite; Cationic substitution; Noble-metal-free; Exsolution; Highly dispersed Cu species

Abstract

Hydroxyapatite ($Ca_{10}(PO_4)_6(OH)_2$, or HAp) – the main mineral component of bones and teeth – is a material of great interest not only in biomedical applications but also in heterogeneous catalysis. Its framework Ca^{2+} cations can be substituted by a wide variety of catalytically active metals (Cu^{2+}, Ni^{2+}, Ag^{+}, etc.). In the present work, for the first time, to our knowledge, we demonstrate that highly valuable HAp-based catalysts can be obtained through a novel advantageous bottom-up approach. Unlike classical surface cation deposition in the excess of solution, this approach is one-pot. It consists in preparing the bulk-metal-substituted HAp by co-precipitation, and then submitting it to a finely adjusted thermal treatment under a H_2-containing gas flow. For a Cu(~1.5wt%)-HAp, we show that such a treatment at 450 °C leads to the exsolution of the whole Cu contained in the material, leading to highly dispersed Cu species at the HAp surface. After appropriate activation, these Cu species are active in the selective catalytic reduction of NO_x by NH_3. The phenomenon of exsolution was reported so far mainly for perovskites, but to lead to metal nanoparticles, not to highly dispersed species as achieved here.

1. Introduction

Hydroxyapatite ($Ca_{10}(PO_4)_6(OH)_2$, or HAp) is a biocompatible and ecological material. As the main mineral component of bones and teeth, it can be obtained from natural sources, or it can be synthesized in mild conditions from cheap precursors.[1,2,3] Besides playing an important role in many clinical applications such as drug design and bone tissue regeneration,[4] it has proved to be efficient as a support and (co-)active phase in heterogeneous catalysis.[1,3,5,6,7] It has important advantages over other materials used in the latter field. Its specific surface area is higher than that of perovskites,[8,9] while its thermal and chemical stabilities are generally better than those of zeolites and metal-organic frameworks.[1,10,11] Its

intrinsic surface acid-base properties can easily be tuned by varying its Ca/P ratio,[12,13,14] and its framework Ca^{2+} cations can be substituted by catalytically active metals (Cu^{2+}, Ni^{2+}, Ag^{+}, etc.).[1,3,15] This leads to multifunctional catalysts suitable for a wide range of applications.[1,3,5] Through surface cation deposition in the excess of solution or strong electrostatic adsorption (SEA), at substituent metal contents of 1-2wt%, it is possible to obtain HAp catalysts with atomically dispersed active sites showing a particularly high catalytic performance and an exceptional resistance to sintering under harsh reaction conditions.[16,17,18]

In the present work, for the first time, to our knowledge, we demonstrate that such highly valuable HAp-based catalysts with highly dispersed active sites can actually be obtained through an advantageous novel bottom-up approach. Unlike surface cation deposition in the excess of solution, this novel approach is one-pot. It involves a phenomenon called "exsolution" that was firstly reported over perovskites.[19] The latter phenomenon consists in the migration of metals incorporated on bulk sites of the perovskite towards the surface under a reducing atmosphere at temperatures above 800 °C. It leads to metal nanoparticles with a size depending on the latter temperature, which are socketed on the perovskite surface, and thus unable to agglomerate.[19] In the case of metal-substituted phosphates ((Sr or Ca)$_{10-x}$M$_x$(PO$_4$)$_6$(OH)$_2$ with M being the Sr^{2+} or Ca^{2+}-substituting metal), the possibility of metal migration from the bulk towards the surface was briefly suggested in earlier studies of Yoon and co-workers.[20,21,22] In these works, Ni-calcium phosphate, Ni-HAp and Ni-strontium phosphate catalysts prepared by co-precipitation were progressively heated from 400 to 800 °C under a partial oxidation of methane (POM) reaction flow (CH_4+O_2/Ar). Based on transmission electron microscopy (TEM) images and associated energy dispersive spectroscopy before and after reaction, the authors concluded that Ni came out of the bulk of the catalysts under reaction conditions, leading to Ni metal particles of a few nanometers at the surface. With increasing temperature, the reaction flow had been progressively enriched with H_2 produced from the POM reaction, indeed. Ultimate evidence of such an exsolution phenomenon exclusively in the Ni-HAp phases, namely the migration of bulk Ni species towards the surface of Ni-HAp under a reducing atmosphere, is difficult to ascertain from the data shown in these studies,[20,21,22] however. The presence of multiple phases, XRD-detectable or not, in these materials greatly complexifies the unravelling of the exsolution phenomenon unequivocally. In particular, the presence of small NiO particles, of which the TEM contrast with the supporting phosphate phase should be much lower than that of corresponding Ni metal particles, could either not be ruled out,[21] or was evidenced through TEM.[22] These NiO particles may be at the origin of the "fine" Ni metal particles observed through TEM after the POM reaction,[21,22] without the involvement of Ni exsolution. In addition, Ni-surface-enrichment after the POM reaction could not be ascertained by XPS because of (i) the overlapping of the Sr 3d and P 2p contributions,[20] and (ii) the fact that no significant difference could be found on the spectra of the Ni-Ca phosphate sample before and after POM reaction.[22] Here, in the case of Cu(~1.5wt%)-HAp materials prepared by co-precipitation, through a combination of surface and bulk characterization techniques, we thoroughly demonstrate that Cu exsolution occurs under a reducing

treatment at only 450 °C, and we assess the extent of that Cu exsolution. We further show that, unlike in the case of perovskites where exsolution leads to nanoparticles at elevated temperatures,[23] the Cu exsolution from Cu-HAp results in highly dispersed Cu at the HAp surface. We finally show how to activate the exsolved Cu for catalyzing the selective catalytic reduction of NO_x by NH_3 (NH_3-SCR), a reaction of great interest for pollution control.[24,25] Exsolving Cu is one step; making it available to act as a catalyst appears to be another step.

2. Experimental section

2.1. Samples preparation

Cu-HAp with the nominal composition $Ca_9Cu_1(PO_4)_6(OH)_2$ was prepared by co-precipitation in an automated reactor (Optimax 1001 synthesis workstation, Mettler Toledo) equipped with integrated pH meter, temperature sensor and mechanical stirrer with adjustable speed, and which offers the possibility to add the precursors solutions at a controlled speed.[8]

Calcium-copper and phosphate solutions were prepared by dissolving 11.54 g of $Ca(NO_3)_2{\cdot}4H_2O$ (Sigma-Aldrich, purity ≥ 99.0%) with 1.32 g of $Cu(NO_3)_2.2.5H_2O$ (Sigma-Aldrich, purity ≥ 99.99%) in 250 mL of ultrapure water, and 3.74 g of $NH_4H_2PO_4$ (Acros Organics, purity ≥ 99.0%) in another 250 mL of ultrapure water, respectively. 200 mL of the latter phosphate solution was then first adjusted to pH 10 by adding a small volume of concentrated ammonia solution (Sigma-Aldrich, 28%) before being poured into the reactor and maintained under an inert atmosphere (N_2). This phosphate solution was then gradually heated up to 80 °C (5 °C/min) under mechanical stirring (400 rpm). Its pH was continuously adjusted to 9 by dropwise adding concentrated ammonia. 200 mL of the calcium-copper solution, beforehand degassed by bubbling N_2 for about 15 minutes and adjusted to pH 10 by adding a few drops of concentrated ammonia, was then poured at a controlled speed (2.2 mL/min) into the reactor. During this step, the pH was kept at 9 by automatically adding appropriate volumes of concentrated ammonia. Once the addition step was completed, a 2 h maturation step at 80 °C and pH 9 was performed. The reactor temperature was finally cooled to 20 °C within a few minutes. The blue precipitate was recovered by centrifugation (8500 rpm) and washed three times with distilled water to mainly remove ammonia, and ammonium and nitrate ions. The wet paste was then recovered on a watch glass and dried overnight at room temperature before the resulting solid was finely ground in an agate mortar.

The recovered Cu-HAp powder was treated under Ar (100 mL/min) at 500 °C (5 °C/min from room temperature) for 1.5 h. As described in Table 1 (section 3.1), the samples that were not later additionally treated under H_2/He are named hereafter Cu-HAp(A), Cu-HAp(B) and Cu-HAp(C) with respect to the synthesis batch from which they originate (A, B or C, respectively). The samples that were later additionally treated under H_2(10%)/He at 450 °C for 1 or 12 h or under H_2(20%)/He at 600 °C for 12 h are named hereafter Cu-HAp(A) 450-1, Cu-HAp(A) 450-12 and Cu-HAp(B) 600-12, respectively. The Cu-HAp(A) 450-1 and Cu-HAp(A) 450-12 samples originate from the synthesis batch A, whereas the

Cu-HAp(B) 600-12 sample originates from the synthesis batch B. The synthesis batch C was used for catalytic tests in the selective catalytic reduction of NO_x by NH_3 (section 2.3).

2.2. Physico-chemical characterization

The actual Cu, Ca and P weight contents of the prepared Cu-HAp were assessed by inductively-coupled plasma optical emission spectroscopy (ICP-OES) with an Agilent 5100 SVDV spectrometer. Samples were mineralized typically as follows. 50 mg of powder was digested with 1 mL of HNO_3 (65% Normatom) at 80-90 °C during 4-6 h and then diluted in 50 mL of ultrapure water. 1 mL of the latter solution was finally diluted by adding HNO_3(2%) until obtaining a total volume of 10 mL. For each analysis, three replicates were performed. Blanks were analyzed to monitor instrument and digestion procedure contamination. Standard solutions were prepared from pluri-elemental and mono-elemental standards (SCP Science) and analyzed for calibration and quality control (drift, reproducibility and accuracy). The concentration of each element (Cu, Ca and P) was calculated as the average of the data recorded at 2 to 5 different wavelengths (for Cu: 213.598, 223.009, 224.700, 324.754 and 327.395 nm; for Ca: 315.887 and 317.933 nm; for P: 178.222 and 213.618 nm).

The specific surface area was evaluated through N_2 physisorption at -196 °C on a BELSORP-max instrument (BEL Japan). Before measurement, the samples were degassed overnight under vacuum (about 10.66 Pa) at 150 °C. The specific surface area was evaluated from the Brunauer-Emmett-Teller (BET) equation ($0.05 < P/P_0 < 0.30$).

Ex situ X-ray diffraction (XRD) under air at room temperature was performed on a Bruker D8 Advance diffractometer equipped with a copper source ($\lambda_{Cu\text{-}K_{\alpha 1}}$ = 1.54056 Å and $\lambda_{Cu\text{-}K_{\alpha 2}}$ = 1.54439 Å) and a LYNXEYE detector. Patterns were recorded in the 2θ range from 15 to 90 °, with a step size of 0.02 ° and a time/step of 0.5 s.

Raman spectra were recorded on a DXR Thermo Scientific spectrometer coupled to an Olympus microscope using a 50 µm slit. A small amount of powder was deposited on a glass slide and flattened with another slide. The slide was then placed on the microscope worktable for analysis. The samples were excited at 532 nm with a laser power of 10 mW through a microscope objective set at a magnification of 50x. The estimated spectral and spatial resolutions were 5.5-8.3 cm^{-1} and 1 µm, respectively.

In situ XRD under He or H_2(10%)/He (30 mL/min) between room temperature and 450 °C was performed on a Bruker D8 Advance diffractometer equipped with a copper source ($\lambda_{Cu\text{-}K_{\alpha 1}}$ = 1.54056 Å and $\lambda_{Cu\text{-}K_{\alpha 2}}$ = 1.54439 Å), an Anton Paar XRK 900 reactor chamber and a LYNXEYE XE-T detector. Patterns were recorded in the 2θ range from 20 to 55 °, with a step size of 0.02 ° and a time/step of 1 s (28.3 min/pattern). The source was operated at a power of 1200 W (40kV, 30mA).

X-ray photoelectron spectroscopy (XPS) was performed on an Omicron Argus spectrometer equipped with a monochromatic AlKα radiation source (hν = 1486.6 eV) and an electron beam power

of 280 W. Photoelectrons emission was analyzed at a photoelectron collection angle of 45 ° under ultra-high vacuum conditions (≤ 10^{-9} mbar). The general spectrum was measured with a pass energy of 100 eV. Regarding the individual elements, the spectra were measured with a pass energy of 20 eV. The area of the C 1s, O 1s, P 2p and Ca 2p peaks was determined with a linear background, and that of the Cu 2p peak was determined with a U 2 Tougaard background. The atomic ratio calculations were performed after normalization using Scofield factors.[26] Spectrum processing was carried out using the Casa XPS software package. In order to determine the standard deviation of the calculated atomic ratios, one sample was analyzed at three different spots (whereas all the other samples were analyzed at one single spot).

Cycles of temperature programmed reduction (TPR) under H_2(5%)/He (25 mL/min) followed by temperature programmed oxidation (TPO) under O_2(5%)/He (25 mL/min) were performed on an AutoChem 2910 instrument. The sample (100 mg) was pre-treated *in situ* under O_2(5%)/He (25 mL/min) at 500 °C (10 °C/min from room temperature) for 1 h. TPR and TPO experiments were typically performed by heating the sample from room temperature to 450 °C at 10 °C/min, and then keeping it at 450 °C for 2 h (unless otherwise mentioned) before cooling it back to room temperature.

High-resolution transmission electron microscopy (HR-TEM) was carried out using a JEOL 2100 Plus UHR microscope operating at 200 kV. The powdered samples were dispersed in ethanol, and then, a drop was evaporated on a carbon-coated molybdenum grid. Scanning transmission electron microscopy (STEM) images using a high-angle annular dark-field (HAADF) detector were also acquired. The image contrast in this mode is strongly correlated with the atomic number: heavier elements contribute to brighter contrast (Z-contrast). Analytic investigations were performed with an energy dispersive X-ray (EDX) spectrometer attached to the microscope column.

2.3. Catalytic tests in the selective catalytic reduction of NO_x by NH_3 (NH_3-SCR)

The catalytic activity of the prepared Cu-HAp in the selective catalytic reduction of NO_x by NH_3 (NH_3-SCR) was investigated in a "Sandwich" reactor-cell.[27] The pelletized Cu-HAp (2 cm² area, ~ 20 mg) was heated under Ar (30 mL/min) from room temperature to 450 °C (3 °C/min set heating rate) for 12 h. H_2 (10%) was added to the flow either 2 or 12 h before the end of the dwell time at 450 °C. In any case, following the reducing step at 450 °C, the sample was cooled down to 110 °C under H_2(10%)/Ar (30 mL/min), then flushed under Ar (30 mL/min) at 110 °C before being exposed to a flow of O_2(20%)/Ar (30 mL/min) at 110 °C for 1 h. The sample was then heated to 120 °C (1 °C/min) under Ar (30 mL/min) and re-exposed to a flow of O_2(20%)/Ar (30 mL/min) at 120 °C for 1 h.[25] Finally, after having been flushed under Ar (30 mL/min) at 120 °C, the sample was exposed to the reaction mixture from 120 to 450 °C (3 °C/min set heating rate with 1 h-stops every 50 °C). The reaction mixture consisted of 500 ppm NO, 500 ppm NH_3 and 1% O_2 in Ar (30 mL/min total flow rate).

Before sending the reaction flow to the reactor-cell, the reactants were monitored by mass spectrometry (Quadrupole Pfeiffer Omnistar GSD 301) until their signals were stable. Then, under reaction conditions, the concentration of NO_x (NO and NO_2) in the outlet gas flow was analyzed by chemiluminescence (Thermo-Scientific, model 42 i-HL). The conversion of NO_x was calculated from equation (1), where $(NO_x)_{inlet}$ and $(NO_x)_{outlet}$ are the NO_x concentrations at the inlet and outlet of the reactor, respectively.

$$NOx \text{ conversion } (\%) = \frac{(NOx)\text{inlet} - (NOx)\text{outlet}}{(NOx)\text{inlet}} * 100 \quad (1)$$

It was beforehand checked on another setup[28] that NO does not undergo significant direct decomposition (without the simultaneous conversion of NH_3) within the range of reaction temperatures investigated in the present work.

3. Results and discussion

3.1. Identity of the prepared Cu-HAp samples

Table 1 shows the ICP-OES-measured Cu weight content (%) and (Ca+Cu)/P bulk atomic ratio, as well as the specific surface area (m^2/g) assessed through N_2 physisorption, of the prepared Cu-HAp samples. The latter are named with respect to the synthesis batch from which they originate and to the conditions of the thermal treatment(s) applied following the synthesis.

Table 1. For one and the same Cu-HAp synthesis procedure, name of the different samples with respect to the conditions of the thermal treatment(s) applied following the synthesis, as well as Cu weight content (%) and (Ca+Cu)/P bulk atomic ratios assessed by ICP-OES, specific surface area (m^2/g) assessed through N_2 physisorption, and crystallite size determined from the XRD patterns by using the Debye-Scherrer equation for the (002) diffraction line. For the thermal treatments, samples were heated from room temperature to treatment temperature at (1) 5 °C/min and (2) 10 °C/min. The total flow rates were (1) 100 mL/min and (2) 50 mL/min. For treatment (2), the indicated H_2 content (x%) was introduced at room temperature.

Sample	Post-synthesis thermal treatment			Cu weight content (%)	(Ca+Cu)/P bulk atomic ratio	Specific surface area (m^2/g)	Crystallite size from (002) diffraction line (nm)
	(1) Cleaning	(2) Reducing					
Cu-HAp(A)	Under Ar at 500 °C for 1.5 h	-		1.5	1.65	91	36.9
Cu-HAp(B)				1.2	1.66	84	38.5
Cu-HAp(C)				1.6	1.66	88	39.3
Cu-HAp(A) 450-1		Under H_2(x%)/He	x=10, at 450 °C for 1 h	1.5	1.65	99	38.2
Cu-HAp(A) 450-12			x=10, at 450 °C for 12 h	1.5	1.65	94	38.1
Cu-HAp(B) 600-12			x=20, at 600 °C for 12 h	1.2	1.66	55	36.4

All three Cu-HAp batches (A, B and C) have similar Cu weight contents (1.5, 1.2 and 1.6%, respectively) and a (Ca+Cu)/P bulk atomic ratio of 1.65-1.66 characteristic of the HAp structure.[8] The latter structure was also confirmed by the *ex situ* XRD patterns recorded under air at room temperature before and after the thermal treatments (Figures S1 and S2, respectively, in the Supporting information). These patterns are all matching with the 9-432-ICDD-PDF standard pattern of HAp, without showing additional signals of Cu-containing secondary phases (for instance libethenite - $Cu_2PO_4(OH)$ - reported elsewhere[29]). The partial substitution of Ca^{2+} cations (100 pm diameter) by smaller Cu^{2+} ones (73 pm diameter) in the here applied synthesis procedure does not induce a shrinkage of the HAp lattice that is sufficiently marked to make the HAp XRD pattern significantly shift to higher angles. In the concerned *ex situ* XRD patterns, slight shifts due to the experimental error (different sample holders, slightly different sample heights following sample preparation) prevail. This is why only *in situ* XRD experiments (section 3.2), in which the experimental error is minimized by monitoring changes as a function of the sample treatment without ever renewing the sample preparation, are commented here in relation with Cu exsolution. The latter phenomenon potentially induces an expansion of the HAp lattice, indeed. The crystallite sizes determined from the *ex situ* XRD patterns by using the Debye-Scherrer equation for the (002) diffraction line (Table 1) are essentially unaffected by the reducing treatments. The 2θ and full width at half maximum values used for the calculations are provided in Table S1. The presence of other apatite phases did not appear from Raman spectroscopy, which revealed no significant difference between the six Cu-HAp samples of Table 1 (spectra in Figures S3 to S5, Supporting information).

The homogeneous distribution of Cu within the material was checked through STEM-EDX analyzes both before and after the reducing treatment at 600 °C (Figures S6 and S7, Supporting information). The fact that the actual Cu weight contents (1.2–1.6%) are lower than the nominal one (6.5 %, corresponding to the nominal composition $Ca_9Cu_1(PO_4)_6(OH)_2$) is attributed to the formation of $[Cu(NH_3)_4]^{2+}$ complexes during the synthesis upon adding NH_4OH to adjust the pH. The Cu-HAp(A), Cu-HAp(B) and Cu-HAp(C) samples have similar specific surface areas (91, 84 and 88 m^2/g, respectively). The reducing treatments at 450 °C do not significantly affect the specific surface area (99 and 94 m^2/g after the 1 h- and 12 h-treatment, respectively, *vs.* 91 m^2/g before treatment). The reducing treatment at 600 °C reduces the specific surface area (55 m^2/g *vs.* 84 m^2/g before treatment). For all samples, the N_2 adsorption-desorption isotherms are provided in Figures S8 and S9.

3.2. Demonstration of Cu exsolution leading to highly dispersed Cu species

Figure 1 shows the XPS-measured Cu/Ca, Cu/P and (Ca+Cu)/P surface atomic ratios of the Cu-HAp(A), Cu-HAp(B), Cu-HAp(A) 450-1, Cu-HAp(A) 450-12 and Cu-HAp(B) 600-12 samples defined in Table 1. The raw XPS spectra are provided in Figures S10 to S14.

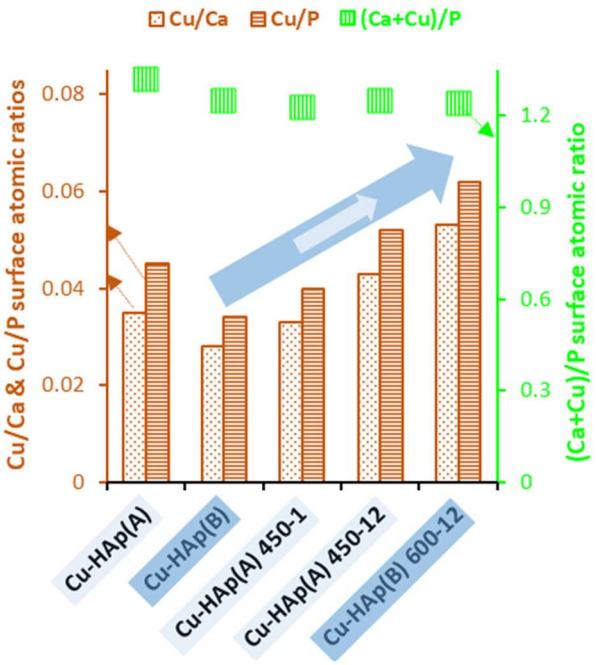

Figure 1. XPS-measured Cu/Ca, Cu/P and (Ca+Cu)/P surface atomic ratios of Cu-HAp samples differing by the post-synthesis thermal treatment(s) they have undergone. The corresponding standard deviations are 0.0009, 0.0006 and 0.049, respectively, as determined by analyzing the Cu-HAp(B) sample at 3 different spots. All samples were first treated under Ar (100 mL/min) at 500 °C (5 °C/min from room temperature) for 1.5 h. The Cu-HAp(A) 450-1, Cu-HAp(A) 450-12 and Cu-HAp(B) 600-12 samples were later additionally treated under H_2(10-20%)/He at 450 °C for 1 or 12 h or at 600 °C for 12 h, respectively, as further detailed in Table 1.

The (Ca+Cu)/P surface atomic ratios (~ 1.3) appear to be significantly lower than those expected from the bulk composition of the materials (1.65-1.66, Table 1). This discrepancy may be assigned to differences in surface composition of the HAp materials, with the preferential exposure of phosphate groups rather than Cu^{2+} and/or Ca^{2+} cations, as compared to the bulk composition.[6] The Cu-HAp(A) 450-1 sample has lower (Ca+Cu)/P, Cu/Ca and Cu/P surface atomic ratios than the Cu-HAp(A) one originating from the same synthesis batch (A) but not having been treated under H_2/He (1.23, 0.033 and 0.040 *vs.* 1.32, 0.035 and 0.045, respectively). This reflects the creation of structural defects under reducing treatment. Interestingly, while the Cu-HAp(A) 450-1 and the Cu-HAp(A) 450-12 samples – treated under H_2(10%)/He at 450 °C for 1 and 12 h, respectively – have nearly the same (Ca+Cu)/P surface ratio (1.23 *vs.* 1.25, respectively), the Cu-HAp(A) 450-12 sample has significantly higher Cu/Ca and Cu/P surface ratios than the Cu-HAp(A) 450-1 one (0.043 and 0.052 *vs.* 0.033 and 0.040, respectively). This indicates that, within the additional 11 h of treatment under H_2(10%)/He at 450 °C to which the Cu-HAp(A) 450-12 sample was submitted, the surface of the latter was Cu-enriched and Ca-depleted. This in turn suggests that Cu^{2+} cations migrated from the Cu-HAp bulk towards the surface, with Ca^{2+} migrating at the opposite from the Cu-HAp surface into the bulk. In other words, Cu exsolution occurs with time upon treating a Cu(1.5wt%)-HAp under H_2(10%)/He at 450 °C.

An even higher increase of the Cu/Ca and Cu/P surface ratios is observed from the Cu-HAp(B) sample to the Cu-HAp(B) 600-12 one (0.028 and 0.034 *vs.* 0.053 and 0.062, respectively), at nearly constant (Ca+Cu)/P ratio (1.25 *vs.* 1.24, respectively). Both samples originate from the same synthesis batch (B),

but only the Cu-HAp(B) 600-12 sample was treated under H_2/He (at 600 °C for 12 h). The Cu-HAp(B) 600-12 sample ends up with higher Cu/Ca and Cu/P ratios than the Cu-HAp(A) 450-12 sample (0.053 and 0.062 *vs.* 0.043 and 0.052, respectively), while both samples have nearly the same (Ca+Cu)/P ratio (1.24 *vs.* 1.25, respectively). This increase of Cu/Ca and Cu/P ratios from the Cu-HAp(A) 450-12 sample to the Cu-HAp(B) 600-12 one appears even more significant considering that the counterpart of Cu-HAp(B) 600-12 before reducing treatment (Cu-HAp(B)) has lower Cu/Ca and Cu/P ratios than the counterpart of Cu-HAp(A) 450-12 before reducing treatment (Cu-HAp(A)) (0.028 and 0.034 *vs.* 0.035 and 0.045, respectively). It indicates that Cu exsolution occurs to a higher extent under H_2(20%)/He at 600 °C than under H_2(10%)/He at 450 °C. To distinguish between the impacts of the H_2 concentration and the treatment temperature was not the goal here.

The data of TPR-TPO cycles applied to the Cu-HAp(A) sample are also consistent with Cu exsolution from the Cu-HAp structure under prolonged reducing treatment. These data further allowed quantifying the extent of exsolution in the considered temperature range. Figure 2 shows the molar ratios of H_2 consumed over Cu contained in the sample (H_2/Cu) and O consumed over Cu contained in the sample (O/Cu) in three successive TPR-TPO cycles on the same Cu-HAp(A) sample. The sample (100 mg) was pre-treated *in situ* under O_2(5%)/He (25 mL/min) at 500 °C (10 °C/min from room temperature) for 1 h. TPR and TPO experiments were then alternately performed under H_2(5%)/He (25 mL/min) and O_2(5%)/He (25 mL/min), respectively. Each TPR experiment was immediately followed by a TPO one before the next TPR experiment was performed. In each TPR/TPO experiment, the sample was heated from room temperature to 450 °C at 10 °C/min, and then left under the reduction or oxidation flow for another 2 h, except in the last TPO experiment. The latter consisted of heating the sample up to 900 °C (10 °C/min) without stop at 450 °C. The H_2 and O_2 consumption profiles as a function of temperature are provided in Figure S15 (Supporting information). The different H_2 and O_2 consumption signals (Figures S15a and S15b, respectively) were quantified *vs.* time as one whole amount of H_2 and O_2 consumed, respectively. It was then considered that every 1 mole of H_2 consumed had reduced 1 mole of Cu^{2+} into Cu^0, and that every ½ mole of O_2 consumed had re-oxidized 1 mole of Cu^0 into Cu^{2+}, respectively.[30,31] Notice that, on the TPR profile of a non-Cu-substituted HAp sample prepared and pre-treated in the same conditions as the Cu-HAp(A) sample (Figure S16), the H_2 consumption is negligible in the here considered temperature range (room temperature to 450 °C, Figure S16a). The only H_2 consumption peak of weak intensity appears at 490 °C (Figure S16b), and may be attributed to H_2 adsorption on an acid-base pair such as Ca^{2+}-O^{2-}, as hydride and proton species.[32]

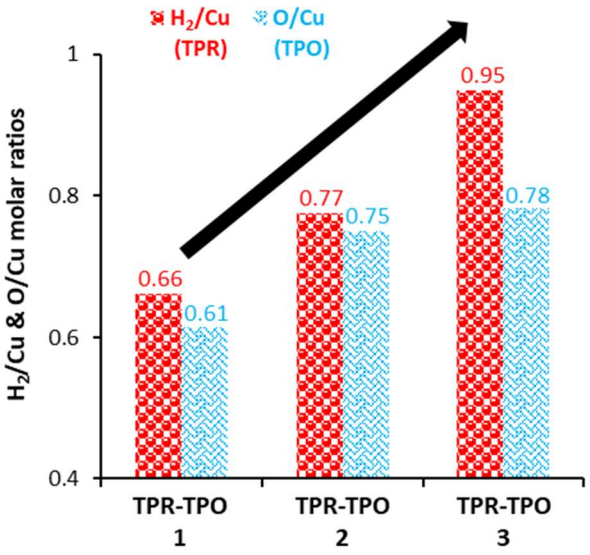

Figure 2. For three successive cycles of temperature programmed reduction (TPR) – temperature programmed oxidation (TPO) on the same Cu-HAp(A) sample, molar ratios of H_2 consumed over Cu contained in the sample (H_2/Cu) and O consumed over Cu contained in the sample (O/Cu). The sample (100 mg) was beforehand treated *ex situ* under Ar (100 mL/min) at 500 °C (5 °C/min from room temperature) for 1.5 h, and then *in situ* under O_2(5%)/He (25 mL/min) at 500 °C (10 °C/min from room temperature) for 1 h. TPR and TPO experiments were then alternately performed under H_2(5%)/He (25 mL/min) and O_2(5%)/He (25 mL/min), respectively. Each TPR experiment was immediately followed by a TPO one before the next TPR experiment was performed. In each TPR/TPO experiment, the sample was heated from room temperature to 450 °C at 10 °C/min, and then left under the reduction or oxidation flow for another 2 h, except in the last TPO experiment. The latter consisted of heating the sample up to 900 °C (10 °C/min) without stop at 450 °C.

The H_2/Cu molar ratio of 0.66 resulting from the first TPR experiment (TPR-TPO cycle 1 in Figure 2) indicates that 66% of the whole Cu^{2+} initially contained in the sample was reduced into Cu^0 within the first TPR. A very close fraction of Cu^0 (61%) was then re-oxidized into Cu^{2+} in the subsequent TPO (still TPR-TPO cycle 1 in Figure 2). Such a high fraction of Cu reduced and then re-oxidized cannot result from the only reduction/oxidation of Cu^{2+}/Cu^0 at the surface of the sample. Cu from the bulk must have been additionally involved. From the first to the second TPR-TPO cycle, the H_2/Cu and O/Cu molar ratios increase to 0.77 and 0.75, respectively. This indicates that the second TPR-TPO experiment led to the reduction/oxidation not only of Cu^{2+} that had already been reduced/oxidized in the first TPR-TPO cycle but also of an additional fraction of Cu species newly accessible to H_2/O_2. The second TPR experiment comprised again a dwell time of 2 h at 450 °C, indeed, which pushed the process of Cu exsolution further. From the second to the third TPR-TPO cycle, only the H_2/Cu molar ratio further increases (from 0.77 to 0.95, respectively). The O/Cu ratio remains nearly the same (0.75 *vs.* 0.78, respectively). Given that the HR-TEM images of Cu-HAp(A) 450-12 do not show Cu particles (Figure 4b), this feature cannot be explained by the exsolution of hardly oxidizable Cu^0 particles in the third TPR experiment. However, it might be ascribed to the fact that the Cu newly exsolved in the third TPR experiment remained in the deepest surface layers or in the near-surface bulk being still accessible to H_2 but not to O_2. While the H_2/Cu ratio in the third TPR experiment (0.95, Figure 2) is already close to 1, suggesting a complete Cu exsolution, the Cu/Ca and Cu/P surface atomic ratios further increase from the Cu-HAp(A) 450-12 sample to the Cu-HAp(B) 600-12 one (Figure 1). This is consistent rather with the hypothesis of exsolved Cu trapped in the near-surface bulk after the reducing treatment at 450 °C.

From the point of view of the Cu-HAp bulk, the exsolution of Cu has a slight impact on the *in situ* XRD patterns of the Cu-HAp(A) sample under a 12 h-exposure to H_2(10%)/Ar (30 mL/min) at 450 °C (Figure 3). The sample was heated from room temperature to 500 °C under He (30 mL/min), at 3 °C/min with 45 min-stops every 50 °C. It was then cooled to 450 °C, and first kept overnight under He (30 mL/min) before being finally exposed to the flow of H_2(10%)/Ar (30 mL/min) for 12 h. Figure 3 shows the XRD patterns that were recorded at 450 °C successively during the first 2.5 h (first 5 patterns in both Figures 3a and 3b, for clarity) and the last 2.5 h (last 5 patterns in Figure 3b) under H_2(10%)/Ar. Figure S17 shows the equivalent patterns recorded in the preceding step at 450 °C under He. All these patterns are shown in the region of the (002) diffraction line which is the sharpest in the *ex situ* pattern of Cu-HAp(A) under air at room temperature (Figure S1a, Supporting information). As compared to the (002) diffraction line in the latter pattern, the (002) diffraction line in Figure 3 and Figure S17 is centered at a slightly smaller angle due to thermal expansion (around 25.72 ° in Figure 3 and Figure S17 *vs.* 25.94 ° in Figure S1a). Such shifts due to thermal expansion are the only changes that were observed on the *in situ* XRD patterns recorded from room temperature to 500 °C under He (Figure S18).

At 450 °C under He (Figure S17), no significant change is observed between the first 5 and the last 5 *in situ* XRD patterns. At 450 °C under H_2(10%)/Ar, on the last 5 patterns (Figure 3b), the maximum of the (002) diffraction line is slightly shifted (about 0.02 °) towards smaller angles corresponding to a slightly expanded HAp lattice, as compared to the first 5 patterns (Figures 3a and 3b). Such an expansion of the HAp lattice evokes the above-concluded migration of Cu^{2+}/Ca^{2+} towards the surface/bulk of the material, as Ca^{2+} cations are wider in diameter than Cu^{2+} ones (100 pm *vs.* 73 pm, respectively). According to the TPR-TPO and XPS data (Figures 2 and 1, respectively), Cu exsolution from the Cu-HAp has indeed occurred to almost 100% after a total of only 6 h under H_2(5%)/He at 450 °C, with a minority fraction of the exsolved Cu being located in the near-surface bulk. In a comparable experiment with non-Cu-substituted HAp, no shift was observed over time at 450 °C under H_2(10%)/Ar (Figure S19).

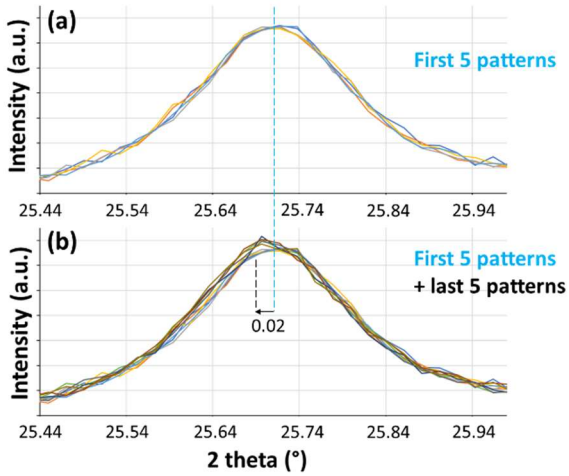

Figure 3. *In situ* XRD patterns of the Cu-HAp(A) sample at 450 °C under H_2(10%)/Ar (30 mL/min) for 12 h, in the region of the (002) diffraction line. The sample - beforehand treated under Ar (100 mL/min) at 500 °C (5 °C/min from room temperature) for 1.5 h - was heated from room temperature to 500 °C under He (30 mL/min), at 3 °C/min with 45 min-stops every 50 °C. The sample was then cooled to 450 °C, and first kept overnight under He (30 mL/min) before being finally exposed to the flow of H_2(10%)/Ar. The XRD patterns were measured successively during the first 2.5 h (first 5 patterns in (a) and (b)) and the last

2.5 h (last 5 patterns in (b)) under H_2(10%)/Ar. Each pattern was measured from 20 to 55 °, with a step size of 0.02 ° and a time/step of 1 s (28.3 min/pattern).

Figure 4 shows HR-TEM images of the Cu-HAp(B) (Figure 4a), Cu-HAp(A) 450-12 (Figure 4b) and Cu-HAp(B) 600-12 (Figures 4c and 4d) samples.

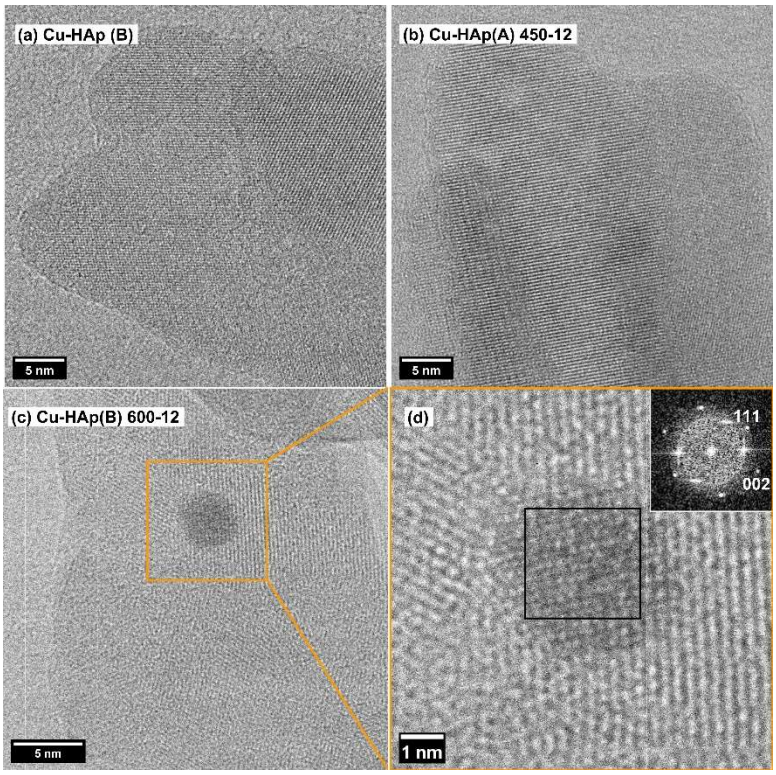

Figure 4. HR-TEM images of three Cu-HAp samples having undergone different post-synthesis thermal treatment(s). In all cases, the samples were first treated under Ar (100 mL/min) at 500 °C (5 °C/min from room temperature) for 1.5 h. In (b) and (c), the samples were additionally treated under H_2(x%)/He (50 mL/min, with x = 10 and 20, respectively) at 450 and 600 °C (10 °C/min from room temperature), respectively, for 12 h (see definition of the sample names in Table 1). In (d), the inset shows the fast Fourier transform (FFT) of the black squared area.

The fact that no Cu particle appears on the Cu-HAp(A) 450-12 sample (Figure 4b) means that a full Cu exsolution at 450 °C leads to highly dispersed Cu species at the surface of the material. Cu particles were observed only for the Cu-HAp(B) 600-12 sample (Figures 4c and 4d) that was treated at a higher temperature than the Cu-HAp(A) 450-12 one (600 *vs.* 450 °C, respectively) and under a higher concentration of H_2 (20 *vs.* 10%, respectively). In Figure 4d, the fast Fourier transform (FFT) of the black squared area shows the characteristic pattern of metallic Cu.[33,34] The FFT of a surrounding area, showing only the characteristic pattern of HAp, is provided in Figure S20. The identity of the Cu particles observed for the Cu-HAp(B) 600-12 sample was further confirmed by STEM-EDX mapping (Figure S21, Supporting information). Typical HR-TEM images of the Cu-HAp(B) 600-12 sample at a lower magnification are provided in Figures S22 and S23 (Supporting information). The diameter of the Cu particles observed in these images ranges from 2.4 to 10.9 nm. No investigation of the particles size distribution is provided since the aim here is to focus on the conditions allowing to get a very high dispersion. The appearance of Cu particles on the Cu-HAp(B) 600-12 sample is not necessarily related

only with Cu exsolution. At a reduction temperature as high as 600 °C, it can also result from the sintering of Cu that was already present at the surface of the material before the reducing treatment.

3.3. Activation of exsolved Cu for catalyzing the NH_3-SCR of NO_x

Reducing treatments at 450 °C as discussed above were performed also as pre-treatments in NH_3-SCR experiments on the Cu-HAp(C) sample. More precisely, the sample was pre-treated *in situ* under Ar then H_2(10%)/Ar (30 mL/min total flow rate) at 450 °C for 12 h before being re-oxidized[25] *in situ* under O_2(20%)/Ar (30 mL/min) at 110 °C for 1 h and then at 120 °C for 1 h. The re-oxidation step was required as Cu needs to be cationic to catalyze the NH_3-SCR.[24,25] Two experiments were performed with different pre-treatment times under H_2(10%)/Ar, namely 2 h *vs.* 12 h. Figure 5 shows the resulting NO_x conversion at 450 °C under a reaction mixture of 500 ppm NO, 500 ppm NH_3 and 1% O_2 in Ar (30 mL/min total flow rate).

As the pre-treatment time under H_2(10%)/Ar increases from 2 to 12 h, the NO_x conversion in Figure 5 increases from 3% to 64%, thus by a factor of 21. On the other hand, in Figure 2, the H_2/Cu molar ratio has already reached 66% at the first TPR and then further increases only by a factor of 1.5, from 66 to 95%, from the first to the third TPR, i.e. as the total time under H_2(5%)/He at 450 °C increases from 2 to 6 h. Furthermore, in Figure S15b, the O_2 consumptions at 120 °C in the first to third TPO experiments are very close. Thus, based on the TPR-TPO data, a partial exsolution treatment of 2 h followed by a re-oxidation at 120 °C should have led to about the same final amount of re-oxidized catalytically active sites as a full exsolution treatment of 6 h or longer followed by the same re-oxidation at 120 °C. This discrepancy between the NH_3-SCR and TPR-TPO data suggests that not all the Cu that was reduced by H_2 in the TPR experiments (Figure 2) and then re-oxidized at 120 °C (Figure S15b), of which the highest fraction resulted from Cu exsolution, was also immediately accessible to the whole reaction mixture (NO_x + NH_3 + O_2) in the NH_3-SCR experiment (Figure 5). Possibly a significant part of the Cu reduced/exsolved at 450 °C in the three successive TPR experiments that was re-oxidized at 120 °C in the subsequent TPO experiments is actually located in deep surface layers where it is not available for converting NO_x by NH_3-SCR. The 12 h-reducing pre-treatment in the NH_3-SCR experiments makes the concerned exsolved Cu truly show-up at the surface, resulting in a significant NO_x conversion (Figure 5).

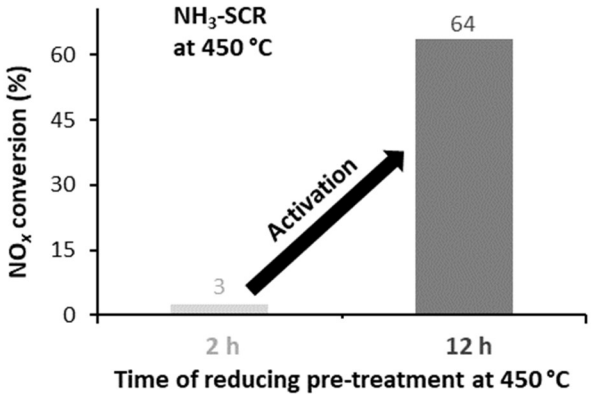

Figure 5. NO_x conversion at 450 °C (with a standard deviation of 0.05%, as calculated over 10 successive values at steady state) in two separate NH_3-SCR experiments on the Cu-HAp(C) sample (20 mg) as a function of the time for which this sample was pre-treated *in situ* under H_2(10%)/Ar (30 mL/min) at 450 °C before being re-oxidized *in situ* under O_2(20%)/Ar (30 mL/min) at 110 °C for 1 h and then at 120 °C for 1 h. The sample was finally exposed to the reaction mixture (500 ppm NO, 500 ppm NH_3 and 1% O_2 in Ar; 30 mL/min total flow rate) from 120 to 450 °C (3 °C/min set heating rate with 1 h-stops every 50 °C). In both experiments, the reducing pre-treatment consisted of heating the sample from room temperature to 450 °C (3 °C/min set heating rate) under Ar (30 mL/min) for 12 h. H_2(10%) was added to the flow either 2 or 12 h before the end of the dwell time at 450 °C. Before these NH_3-SCR experiments, the sample had already been treated *ex situ* under Ar (100 mL/min) at 500 °C (5 °C/min from room temperature) for 1.5 h.

4. Conclusions

For the first time, to our knowledge, the present paper demonstrates through a combination of surface and bulk characterization techniques that a metal, here Cu, can exsolve from a bulk-metal-substituted HAp, here Cu(1.5wt%)-HAp synthesized by co-precipitation. About 66% of the whole Cu initially contained in the Cu-HAp is exsolved after 2 h under H_2(5%)/He at a temperature as low as 450 °C; nearly 100% is exsolved after 6 h. A fraction of the exsolved Cu however remains in deep surface layers/the near-surface bulk of the material. Therefore, to become available for catalyzing reactions, this exsolved Cu might require a prolonged treatment. Here, in the NH_3-SCR of NO_x at 450 °C, the Cu exsolved after 2 h under H_2(10%)/Ar at 450 °C (at least 66% of the whole Cu initially contained in the material) is not immediately active following a re-oxidation treatment. It becomes active, however, after prolonging the treatment under H_2(10%)/Ar at 450 °C to 12 h followed by the same re-oxidation treatment. The 12 h reducing treatment actually leads to a full Cu exsolution, but keeping the exsolved Cu surface species highly dispersed. Nanoparticles of Cu (2 nm < diameter < 11 nm) appear only after a reducing treatment at higher temperature and/or higher H_2 concentration, as observed for a Cu-HAp sample treated under H_2(20%)/He at 600 °C for 12 h.

The present work shows that reaching a 1.5wt% surface content of highly dispersed Cu on HAp does not require a two-pot synthesis approach such as precipitation of the HAp followed by Cu^{2+} deposition in the excess of solution. Such a surface content of highly dispersed Cu can be achieved through a one-pot synthesis approach, namely co-precipitation of the Cu-HAp followed by H_2-treatment for Cu exsolution. As this approach is *a priori* not restricted to only Cu as the catalytically active metal, the present work constitutes a considerable step forward in the development of efficient routes for the design of highly active HAp-based catalysts.

Supporting information

Ex situ XRD patterns in the 2 theta region from 15 to 90 ° of all Cu-HAp samples under air at room temperature; Crystallite size of all samples calculated by using the Scherrer equation for the (002) diffraction line *;* Raman spectra of all samples under air at room temperature; HR-TEM and STEM-HAADF images of the Cu-HAp(B) 600-12 sample with corresponding STEM-EDX maps; HR-TEM images of the Cu-HAp(B) 600-12 sample at a lower magnification for an overview of the size of Cu particles; STEM-HAADF image of the Cu-HAp(B) reference sample with corresponding STEM-EDX maps; N_2 adsorption-desorption isotherms for all Cu-HAp samples; XPS spectra of all samples; H_2 consumption and O_2 consumption profiles in three successive H_2-TPR – O_2-TPO cycles on the same Cu-HAp(A) sample; H_2 consumption profile in the TPR experiment performed on a non-Cu-substituted HAp sample; *In situ* XRD patterns of the Cu-HAp(A) sample upon heating from 30 to 500 °C under He and then upon keeping the sample overnight at 450 °C under He; *In situ* XRD patterns of a non-Cu-substituted HAp sample at 450 °C under H_2(10%)/Ar.

Acknowledgements

This work has benefited from a funding managed by the French National Research Agency (DECOMPNOx project: ANR-18-CE07-0002) as well as from a funding of the French Council for Scientific Research (CNRS) granted to newly hired permanent researchers (Josefine Schnee). The TEM microscope is a facility of the Chemistry and Materials Federation of Paris-Centre (FCMat) and was funded by Sorbonne Université, CNRS and Région Ile-de-France, which are gratefully acknowledged. The authors also acknowledge Saremblé Guira and Frédéric Averseng (Sorbonne Université, CNRS, Laboratoire de Réactivité de Surface, Paris, France) for running a part of the N_2 physisorption measurements and for fruitful discussions, respectively, as well as Philippe Bazin (Normandie Université, CNRS, Laboratoire Catalyse et Spectrochimie, Caen, France) for his technical support in the NH_3-SCR experiments.

Author information

Corresponding authors

*E-mails: josefine.schnee@sorbonne-universite.fr, cyril.thomas@sorbonne-universite.fr

ORCID numbers

Josefine Schnee: 0000-0001-8521-9922

Ferdaous Ben Romdhane: 0000-0002-3502-3056

François Devred: 0000-0002-7510-1581

Antoine Miche: 0000-0002-8006-1123

Alixandre Magerat: 0000-0001-9480-3549

Eric M. Gaigneaux: 0000-0003-2239-4306

Marco Daturi: 0000-0001-5147-3260

Cyril Thomas: 0000-0003-4224-6095

Guylène Costentin: 0000-0003-1559-6890

Competing interests

The authors declare no competing interests.

References

1. Ibrahim, M.; Labaki, M.; Giraudon, J.-M.; Lamonier, J.-F., Hydroxyapatite, a multifunctional material for air, water and soil pollution control: A review. *Journal of Hazardous Materials* **2020,** *383*, 121139.
2. Campisi, S.; Galloni, M. G.; Bossola, F.; Gervasini, A., Comparative performance of copper and iron functionalized hydroxyapatite catalysts in NH3-SCR. *Catal. Commun.* **2019,** *123*, 79-85.
3. Fihri, A.; Len, C.; Varma, R. S.; Solhy, A., Hydroxyapatite: A review of syntheses, structure and applications in heterogeneous catalysis. *Coordination Chemistry Reviews* **2017,** *347*, 48-76.
4. Šupová, M., Substituted hydroxyapatites for biomedical applications: A review. *Ceramics International* **2015,** *41* (8), 9203-9231.
5. Minh, D. P., *Design and Applications of Hydroxyapatite-Based Catalysts*. John Wiley & Sons: 2022; p 576.
6. Ben Osman, M.; Diallo Garcia, S.; Krafft, J.-M.; Methivier, C.; Blanchard, J.; Yoshioka, T.; Kubo, J.; Costentin, G., Control of calcium accessibility over hydroxyapatite by post-precipitation steps: influence on the catalytic reactivity toward alcohols. *Physical Chemistry Chemical Physics* **2016,** *18* (40), 27837-27847.
7. Osman, M. B.; Krafft, J.-M.; Thomas, C.; Yoshioka, T.; Kubo, J.; Costentin, G., Importance of the Nature of the Active Acid/Base Pairs of Hydroxyapatite Involved in the Catalytic Transformation of Ethanol to n-Butanol Revealed by Operando DRIFTS. *ChemCatChem* **2019,** *11* (6), 1765-1778.
8. Reynaud, C.; Thomas, C.; Casale, S.; Nowak, S.; Costentin, G., Development of a thermodynamic approach to assist the control of the precipitation of hydroxyapatites and associated calcium phosphates in open systems. *CrystEngComm* **2021,** *23* (27), 4857-4870.
9. Hwang, C.; Gwon, O.; Jo, H.; Ok, K. M.; Kim, G., Major Role of Surface Area in Perovskite Electrocatalysts for Alkaline Systems. *ChemElectroChem* **2017,** *4* (3), 468-471.
10. Cruciani, G., Zeolites upon heating: Factors governing their thermal stability and structural changes. *Journal of Physics and Chemistry of Solids* **2006,** *67* (9), 1973-1994.
11. Escobar-Hernandez, H. U.; Pérez, L. M.; Hu, P.; Soto, F. A.; Papadaki, M. I.; Zhou, H.-C.; Wang, Q., Thermal Stability of Metal–Organic Frameworks (MOFs): Concept, Determination, and Model Prediction Using Computational Chemistry and Machine Learning. *Industrial & Engineering Chemistry Research* **2022,** *61* (17), 5853-5862.
12. Ma, Z., Hydroxyapatite-Based Catalysts: Influence of the Molar Ratio of Ca to P. In *Design and Applications of Hydroxyapatite-Based Catalysts*, Minh, D. P., Ed. John Wiley & Sons: 2022; pp 141-161.
13. Tsuchida, T.; Kubo, J.; Yoshioka, T.; Sakuma, S.; Takeguchi, T.; Ueda, W., Influence of Preparation Factors on Ca/P Ratio and Surface Basicity of Hydroxyapatite Catalyst. *Journal of the Japan Petroleum Institute* **2009,** *52* (2), 51-59.
14. Diallo-Garcia, S.; Osman, M. B.; Krafft, J.-M.; Casale, S.; Thomas, C.; Kubo, J.; Costentin, G., Identification of Surface Basic Sites and Acid–Base Pairs of Hydroxyapatite. *The Journal of Physical Chemistry C* **2014,** *118* (24), 12744-12757.

15. Costentin, G.; Drouet, C.; Salles, F.; Sarda, S., Structure and Surface Study of Hydroxyapatite-Based Materials: Experimental and Computational Approaches. In *Design and Applications of Hydroxyapatite-Based Catalysts*, Minh, D. P., Ed. John Wiley & Sons: 2022; pp 73-140.
16. Akri, M.; Zhao, S.; Li, X.; Zang, K.; Lee, A. F.; Isaacs, M. A.; Xi, W.; Gangarajula, Y.; Luo, J.; Ren, Y.; Cui, Y.-T.; Li, L.; Su, Y.; Pan, X.; Wen, W.; Pan, Y.; Wilson, K.; Li, L.; Qiao, B.; Ishii, H.; Liao, Y.-F.; Wang, A.; Wang, X.; Zhang, T., Atomically dispersed nickel as coke-resistant active sites for methane dry reforming. *Nature Communications* **2019,** *10* (1), 5181.
17. Mori, K.; Mitani, Y.; Hara, T.; Mizugaki, T.; Ebitani, K.; Kaneda, K., A single-site hydroxyapatite-bound zinc catalyst for highly efficient chemical fixation of carbon dioxide with epoxides. *Chemical Communications* **2005,** (26), 3331-3333.
18. Mori, K.; Oshiba, M.; Hara, T.; Mizugaki, T.; Ebitani, K.; Kaneda, K., Creation of monomeric La complexes on apatite surfaces and their application as heterogeneous catalysts for Michael reactions. *New Journal of Chemistry* **2006,** *30* (1), 44-52.
19. Neagu, D.; Irvine, J. T. S.; Wang, J.; Yildiz, B.; Opitz, A. K.; Fleig, J.; Wang, Y.; Liu, J.; Shen, L.; Ciucci, F.; Rosen, B. A.; Xiao, Y.; Xie, K.; Yang, G.; Shao, Z.; Zhang, Y.; Reinke, J.; Schmauss, T. A.; Barnett, S. A.; Maring, R.; Kyriakou, V.; Mushtaq, U.; Tsampas, M. N.; Kim, Y.; O'Hayre, R.; Carrillo, A. J.; Ruh, T.; Lindenthal, L.; Schrenk, F.; Rameshan, C.; Papaioannou, E. I.; Kousi, K.; Metcalfe, I. S.; Xu, X.; Liu, G., Roadmap on exsolution for energy applications. *Journal of Physics: Energy* **2023,** *5* (3), 031501.
20. Lee, S. J.; Jun, J. H.; Lee, S.-H.; Yoon, K. J.; Lim, T. H.; Nam, S.-W.; Hong, S.-A., Partial oxidation of methane over nickel-added strontium phosphate. *Applied Catalysis A: General* **2002,** *230* (1), 61-71.
21. Jun, J. H.; Lee, S. J.; Lee, S.-H.; Lee, T.-J.; Kong, S. J.; Lim, T. H.; Nam, S.-W.; Hong, S.-A.; Yoon, K. J., Characterization of a nickel-strontium phosphate catalyst for partial oxidation of methane. *Korean Journal of Chemical Engineering* **2003,** *20* (5), 829-834.
22. Jun, J. H.; Lee, T.-J.; Lim, T. H.; Nam, S.-W.; Hong, S.-A.; Yoon, K. J., Nickel–calcium phosphate/hydroxyapatite catalysts for partial oxidation of methane to syngas: characterization and activation. *Journal of Catalysis* **2004,** *221* (1), 178-190.
23. Kwon, O.; Sengodan, S.; Kim, K.; Kim, G.; Jeong, H. Y.; Shin, J.; Ju, Y.-W.; Han, J. W.; Kim, G., Exsolution trends and co-segregation aspects of self-grown catalyst nanoparticles in perovskites. *Nature Communications* **2017,** *8* (1), 15967.
24. Hamoud, H. I.; Valtchev, V.; Daturi, M., Selective catalytic reduction of NOx over Cu- and Fe-exchanged zeolites and their mechanical mixture. *Applied Catalysis B: Environmental* **2019,** *250*, 419-428.
25. Schiavoni, M.; Campisi, S.; Carniti, P.; Gervasini, A.; Delplanche, T., Focus on the catalytic performances of Cu-functionalized hydroxyapatites in NH3-SCR reaction. *Applied Catalysis A: General* **2018,** *563*, 43-53.
26. Scofield, J. H., Hartree-Slater subshell photoionization cross-sections at 1254 and 1487 eV. *Journal of Electron Spectroscopy and Related Phenomena* **1976,** *8* (2), 129-137.
27. Wuttke, S.; Bazin, P.; Vimont, A.; Serre, C.; Seo, Y.-K.; Hwang, Y. K.; Chang, J.-S.; Férey, G.; Daturi, M., Discovering the Active Sites for C3 Separation in MIL-100(Fe) by Using Operando IR Spectroscopy. *Chemistry – A European Journal* **2012,** *18* (38), 11959-11967.
28. Schnee, J.; Delannoy, L.; Costentin, G.; Thomas, C., Unraveling the Direct Decomposition of NOx over Keggin Heteropolyacids and Their Deactivation Using a Combination of Gas-IR/MS and In Situ DRIFT Spectroscopy. *The Journal of Physical Chemistry C* **2020,** *124* (41), 22459-22470.
29. Carvalho, D. C.; Pinheiro, L. G.; Campos, A.; Millet, E. R. C.; de Sousa, F. F.; Filho, J. M.; Saraiva, G. D.; Filho, E. C. d. S.; Fonseca, M. G.; Oliveira, A. C., Characterization and catalytic performances of copper and cobalt-exchanged hydroxyapatite in glycerol conversion for 1-hydroxyacetone production. *Applied Catalysis A: General* **2014,** *471*, 39-49.
30. Boukha, Z.; Ayastuy, J. L.; Cortés-Reyes, M.; Alemany, L. J.; González-Velasco, J. R.; Gutiérrez-Ortiz, M. A., Catalytic performance of Cu/hydroxyapatite catalysts in CO preferential oxidation in H2-rich stream. *International Journal of Hydrogen Energy* **2019,** *44* (25), 12649-12660.

31. Guo, J.; Yu, H.; Dong, F.; Zhu, B.; Huang, W.; Zhang, S., High efficiency and stability of Au–Cu/hydroxyapatite catalyst for the oxidation of carbon monoxide. *RSC Advances* **2017,** *7* (72), 45420-45431.
32. Petit, S.; Thomas, C.; Millot, Y.; Krafft, J.-M.; Laberty-Robert, C.; Costentin, G., Activation of C−H Bond of Propane by Strong Basic Sites Generated by Bulk Proton Conduction on V-Modified Hydroxyapatites for the Formation of Propene. *ChemCatChem* **2020,** *12* (9), 2506-2521.
33. Yonezawa, T.; Uchida, Y.; Tsukamoto, H., X-ray diffraction and high-resolution TEM observations of biopolymer nanoskin-covered metallic copper fine particles: preparative conditions and surface oxidation states. *Physical Chemistry Chemical Physics* **2015,** *17* (48), 32511-32516.
34. Cheng, G.; Hight Walker, A. R., Transmission electron microscopy characterization of colloidal copper nanoparticles and their chemical reactivity. *Analytical and Bioanalytical Chemistry* **2010,** *396* (3), 1057-1069.

TOC graphical abstract

Hydroxyapatite: a matrix for metal exsolution leading to highly dispersed catalytically active species

Josefine Schnee,[a,*] Ferdaous Ben Romdhane,[b] François Devred,[c] Antoine Miche,[a] Alixandre Magerat,[c] Diane Reja,[a] Eric M. Gaigneaux,[c] Marco Daturi,[d] Cyril Thomas[a,*] and Guylène Costentin[a]

[a]Sorbonne Université, CNRS, Laboratoire de Réactivité de Surface (LRS), Campus Pierre et Marie Curie, 4 Place Jussieu, F-75005 Paris, France.
[b]Fédération de Chimie et Matériaux de Paris-Centre (FCMat), Campus Pierre et Marie Curie, 4 Place Jussieu, F-75005 Paris, France.
[c]Université catholique de Louvain, Institute of Condensed Matter and Nanosciences (IMCN), Molecular Chemistry, Materials and Catalysis (MOST), Place Louis Pasteur 1 box L4.01.09, B-1348 Louvain-la-Neuve, Belgium.
[d]Normandie Université, ENSICAEN, UNICAEN, CNRS, Laboratoire Catalyse et Spectrochimie, 6 Boulevard Maréchal Juin, F-14050 Caen, France.
*Corresponding authors: josefine.schnee@sorbonne-universite.fr, cyril.thomas@sorbonne-universite.fr.

Supporting information

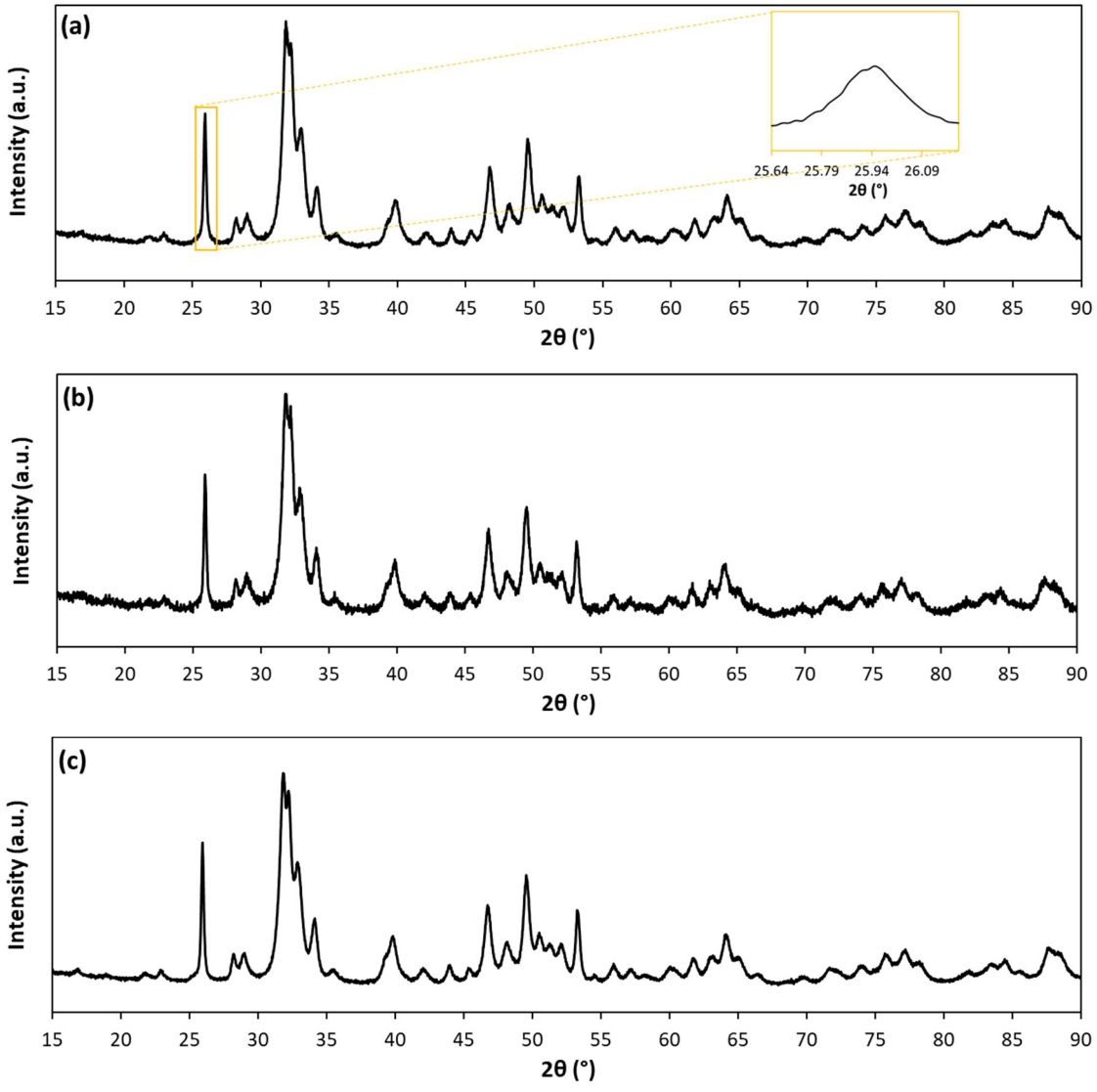

Figure S1. *Ex situ* XRD patterns of the Cu-HAp(A) (a), Cu-HAp(B) (b) and Cu-HAp(C) (c) samples under air at room temperature. The inset in (a) focuses on the (002) diffraction line.

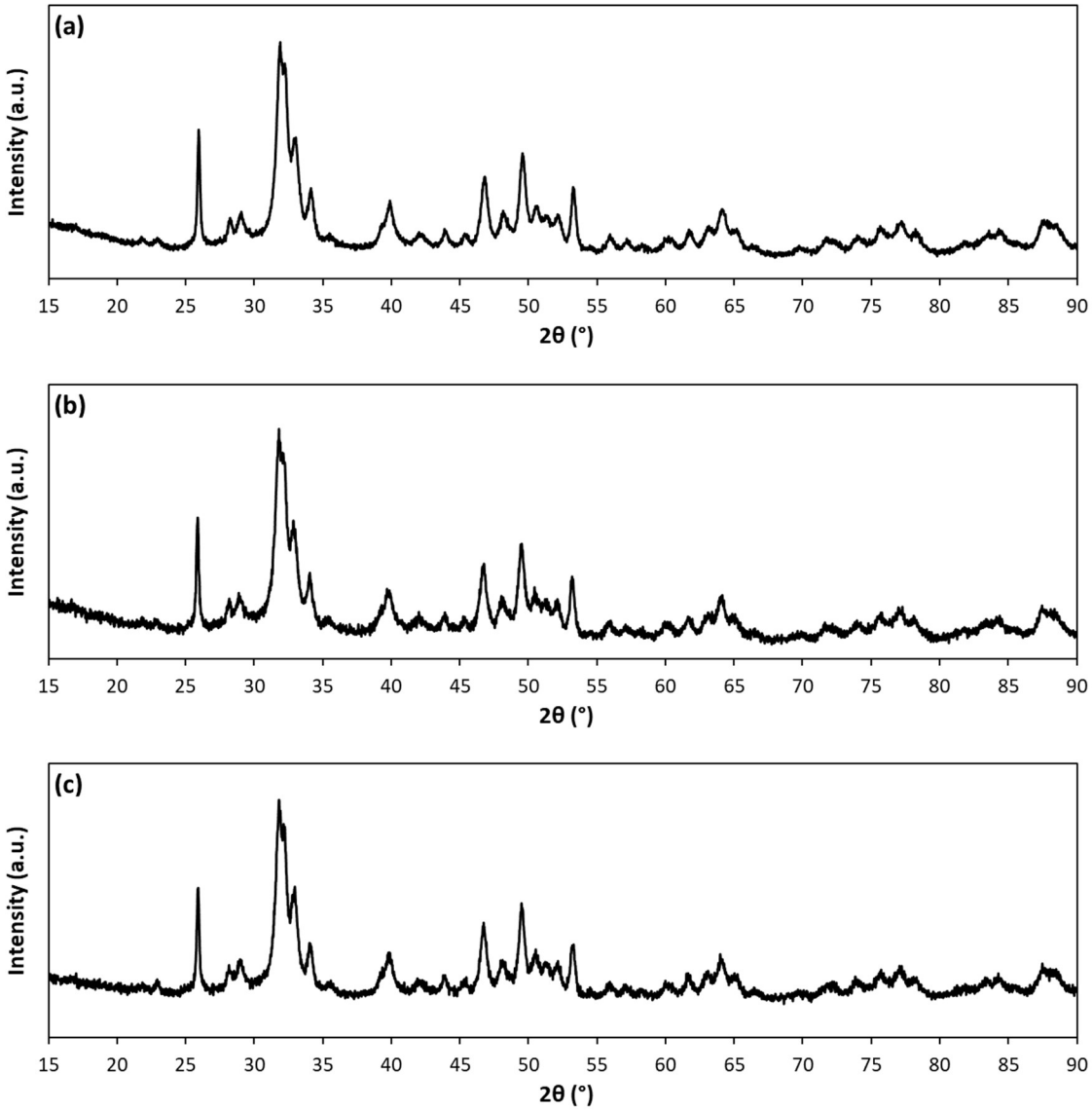

Figure S2. *Ex situ* XRD patterns of the Cu-HAp(A) 450-1 (a), Cu-HAp(A) 450-12 (b) and Cu-HAp(B) 600-12 (c) samples under air at room temperature.

Table S1. Crystallite size of all samples calculated by using the Scherrer equation for the (002) diffraction line (FWHM = full width at half maximum).

Sample	2θ (°)	FWHM (°)	Crystallite size (nm)
Cu-HAp(A)	25.93	0.22	36.9
Cu-HAp(B)	25.93	0.21	38.5
Cu-HAp(C)	25.94	0.20	39.3
Cu-HAp(A) 450-1	25.94	0.21	38.2
Cu-HAp(A) 450-12	25.88	0.21	38.1
Cu-HAp(B) 600-12	25.89	0.22	36.4

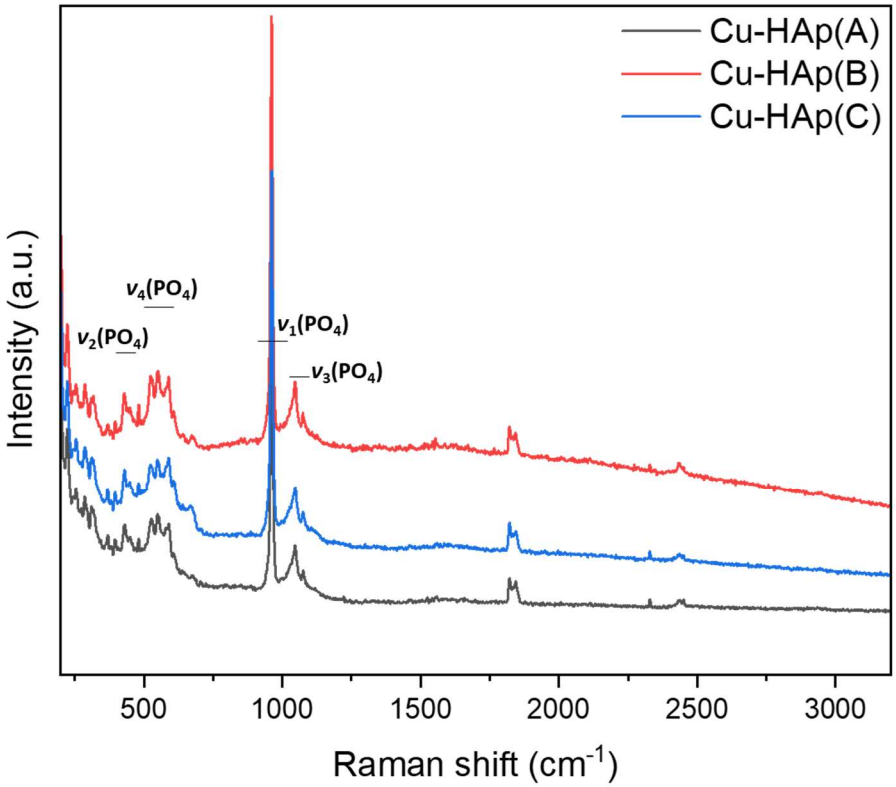

Figure S3. Raman spectra of the Cu-HAp(A), Cu-HAp(B) and Cu-HAp(C) samples under air at room temperature.

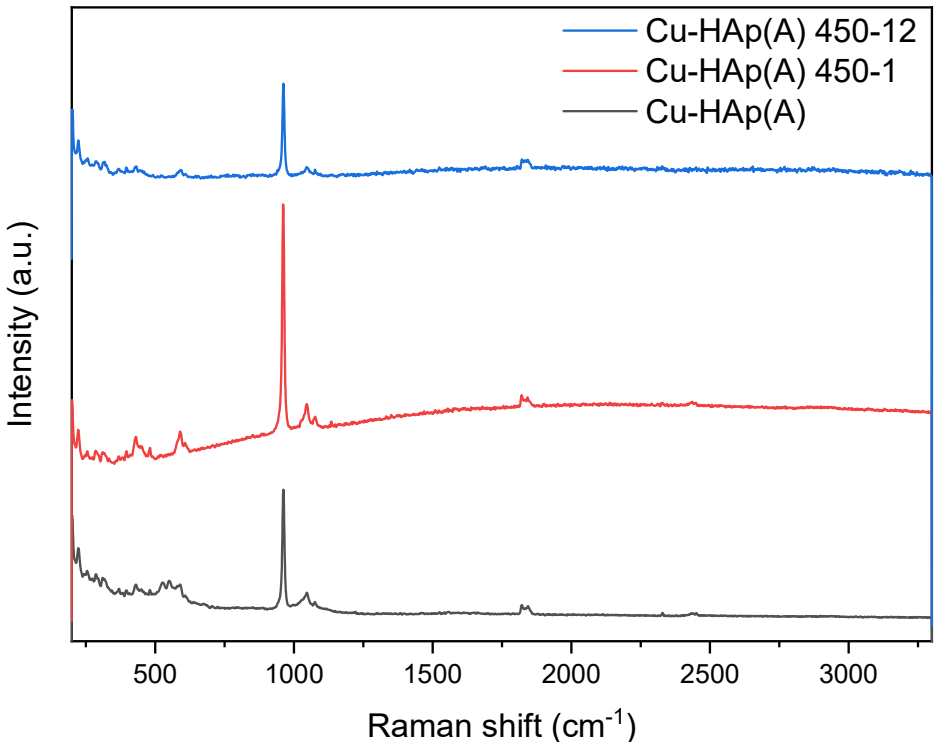

Figure S4. Raman spectra of the Cu-HAp(A), Cu-HAp(A) 450-1 and Cu-HAp(A) 450-12 samples under air at room temperature.

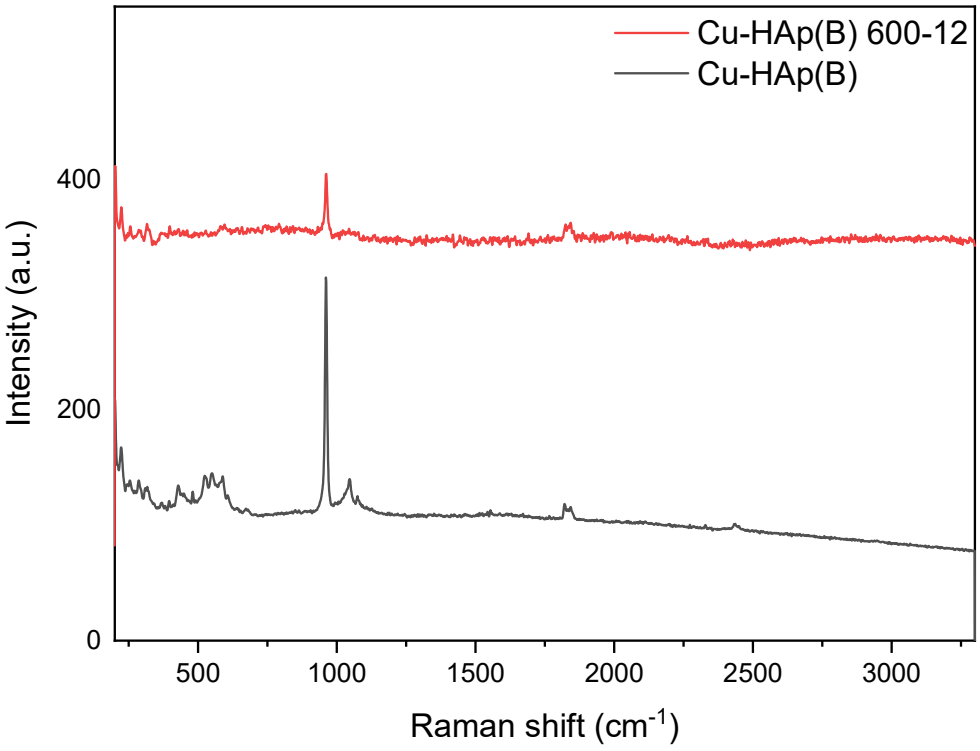

Figure S5. Raman spectra of the Cu-HAp(B) and Cu-HAp(B) 600-12 samples under air at room temperature.

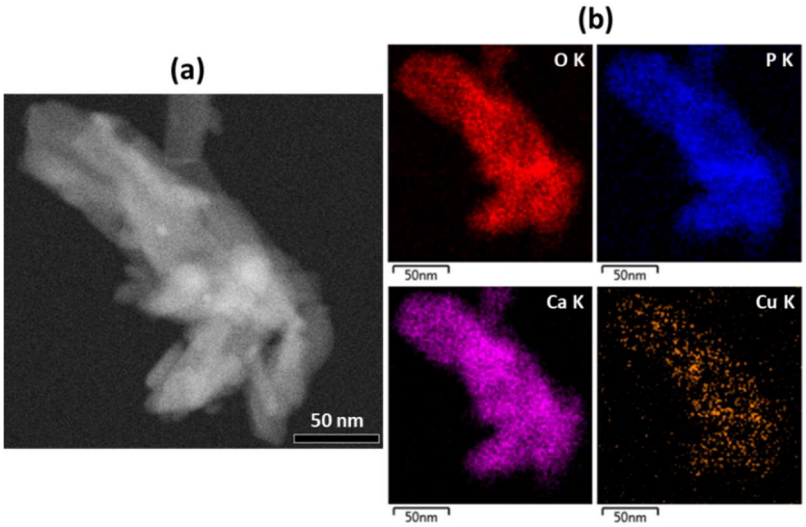

Figure S6. (a) STEM-HAADF image of the Cu-HAp(B) 600-12 sample and (b) corresponding STEM-EDX maps. The sample was beforehand treated first under Ar (100 mL/min) at 500 °C (5 °C/min from room temperature) for 1.5 h, and later under H_2(20%)/He (50 mL/min) at 600 °C for 12 h. In the latter treatment, the sample was heated from room temperature to 600 °C at 10 °C/min already under the H_2(20%)/He flow.

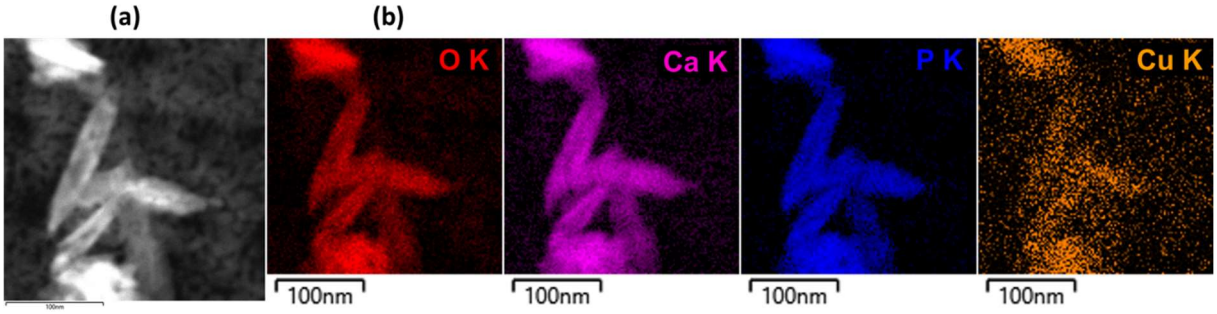

Figure S7. (a) STEM-HAADF image of the Cu-HAp(B) sample and (b) corresponding STEM-EDX maps. The sample was beforehand treated under Ar (100 mL/min) at 500 °C (5 °C/min from room temperature) for 1.5 h.

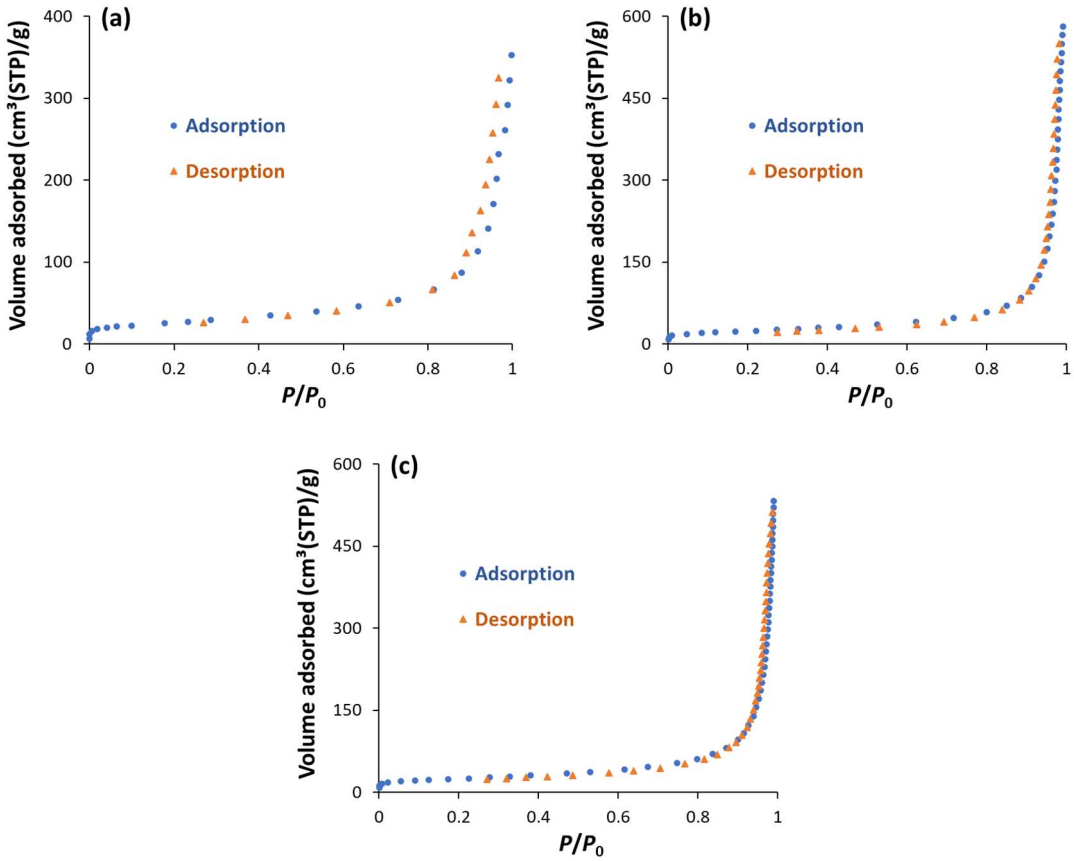

Figure S8. N_2 adsorption-desorption isotherms for the Cu-HAp(A) (a), Cu-HAp(B) (b) and Cu-HAp(C) (c) samples.

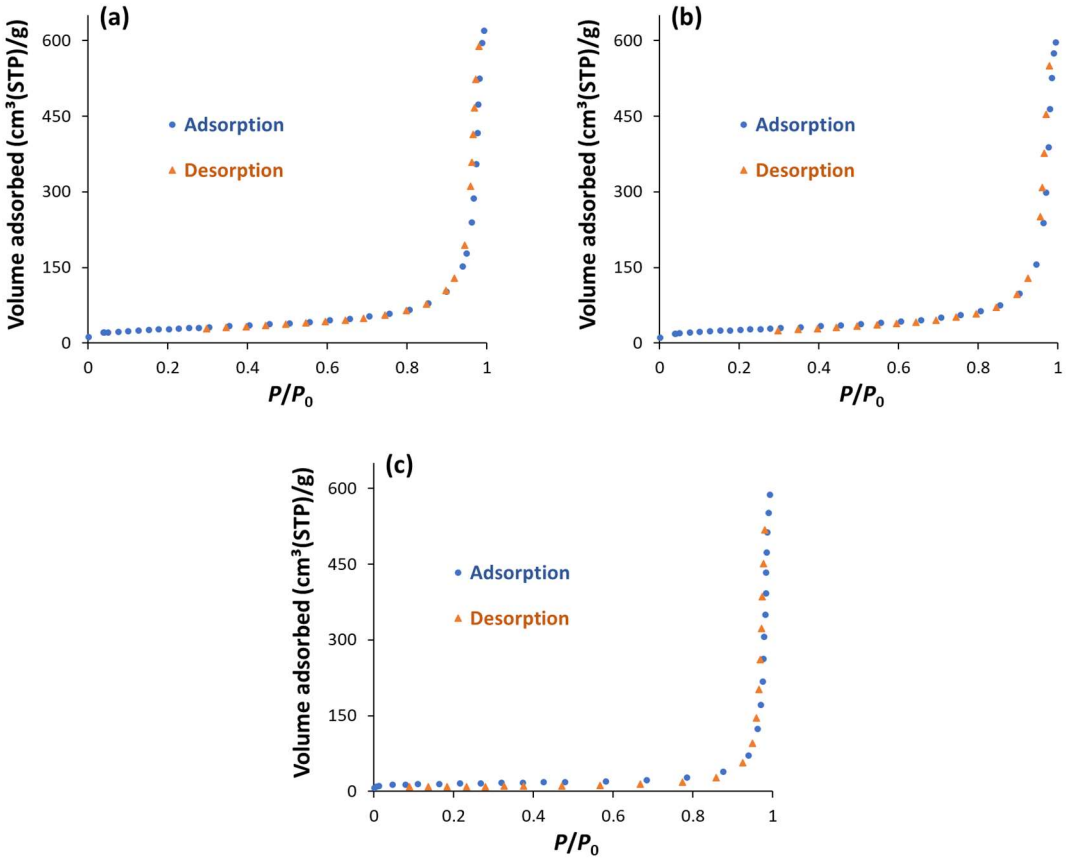

Figure S9. N_2 adsorption-desorption isotherms for the Cu-HAp(A) 450-1 (a), Cu-HAp(A) 450-12 (b) and Cu-HAp(B) 600-12 (c) samples.

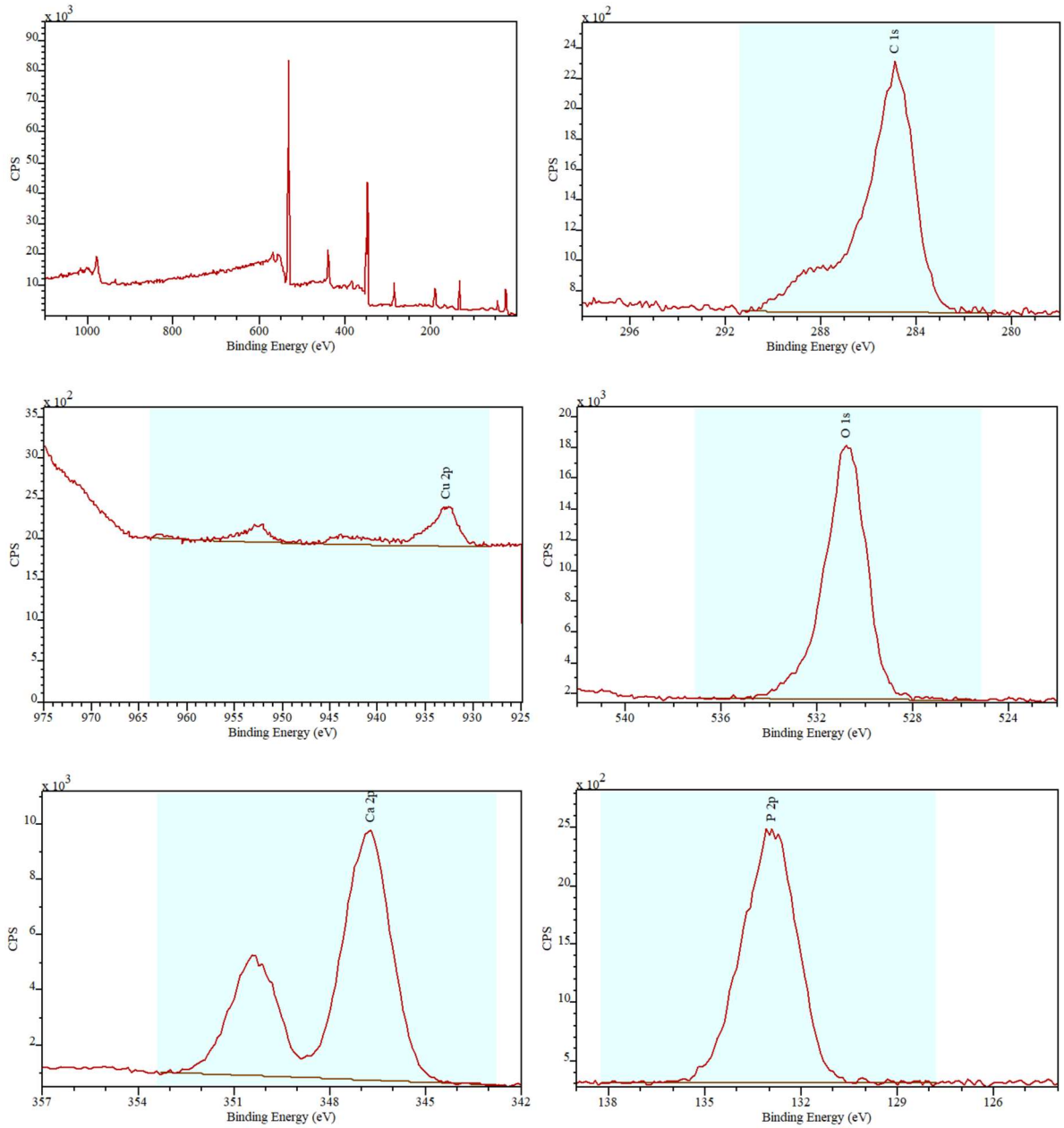

Figure S10. XPS spectra of the Cu-HAp(A) sample.

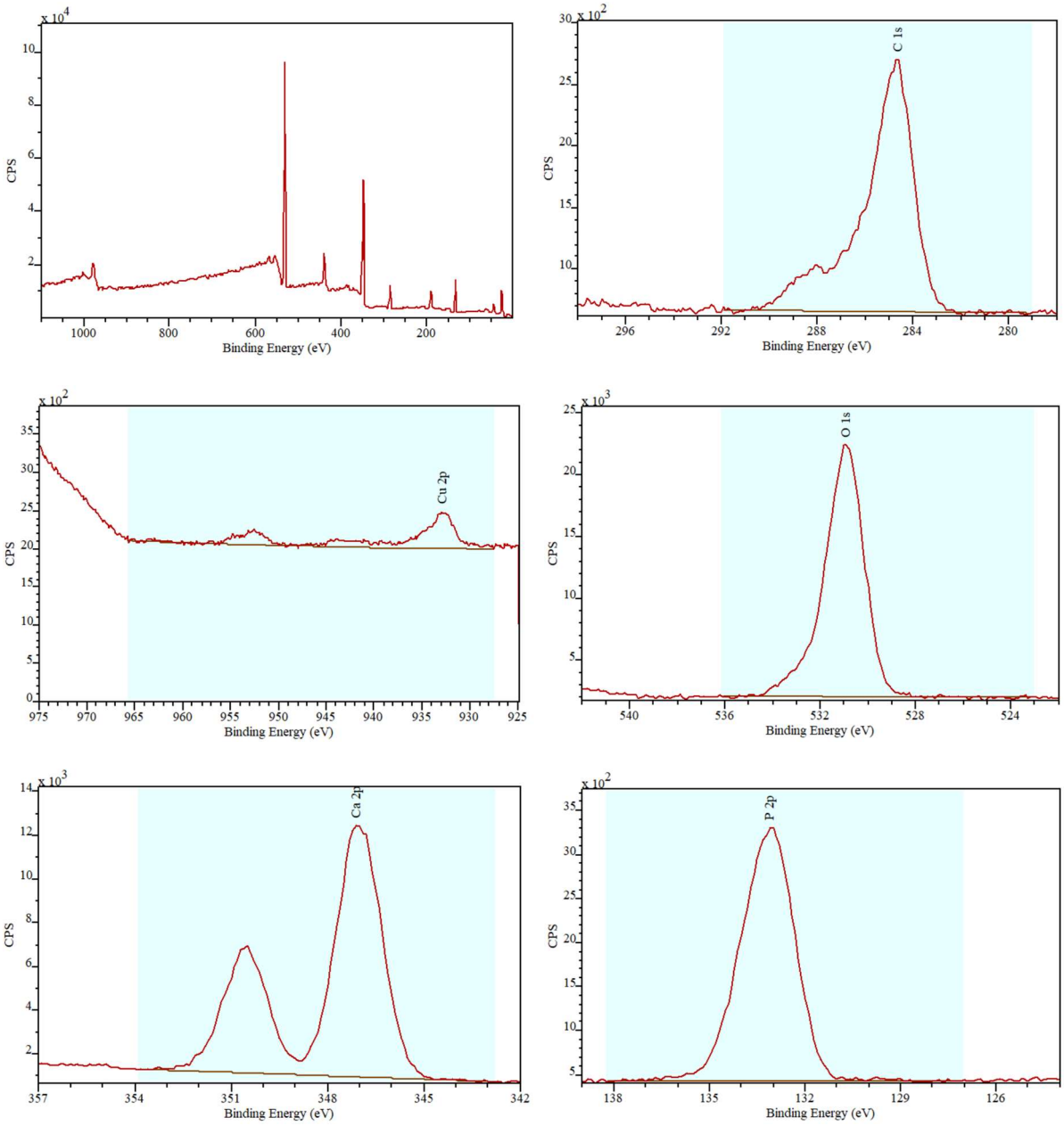

Figure S11. XPS spectra of the Cu-HAp(B) sample.

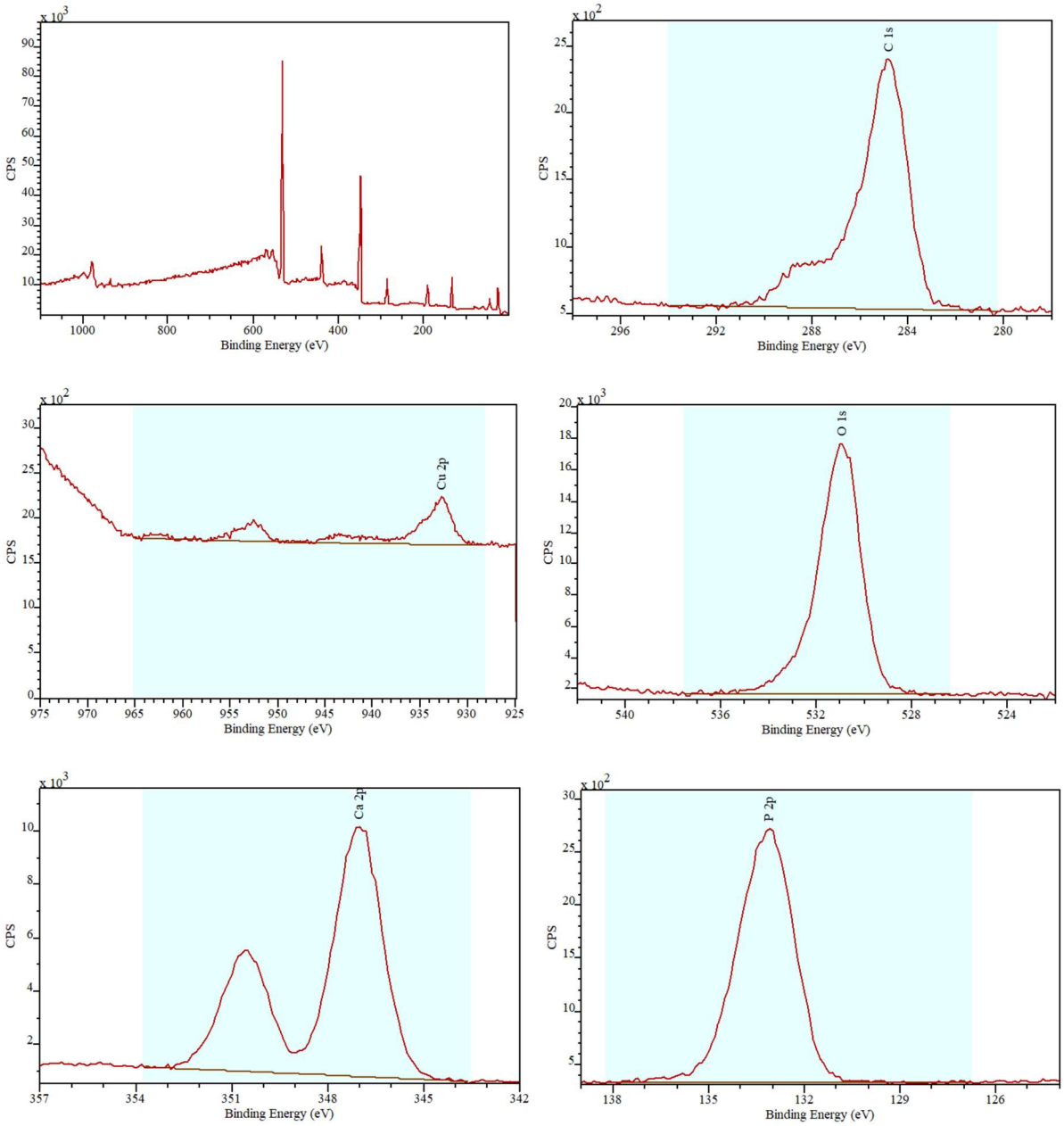

Figure S12. XPS spectra of the Cu-HAp(A) 450-1 sample.

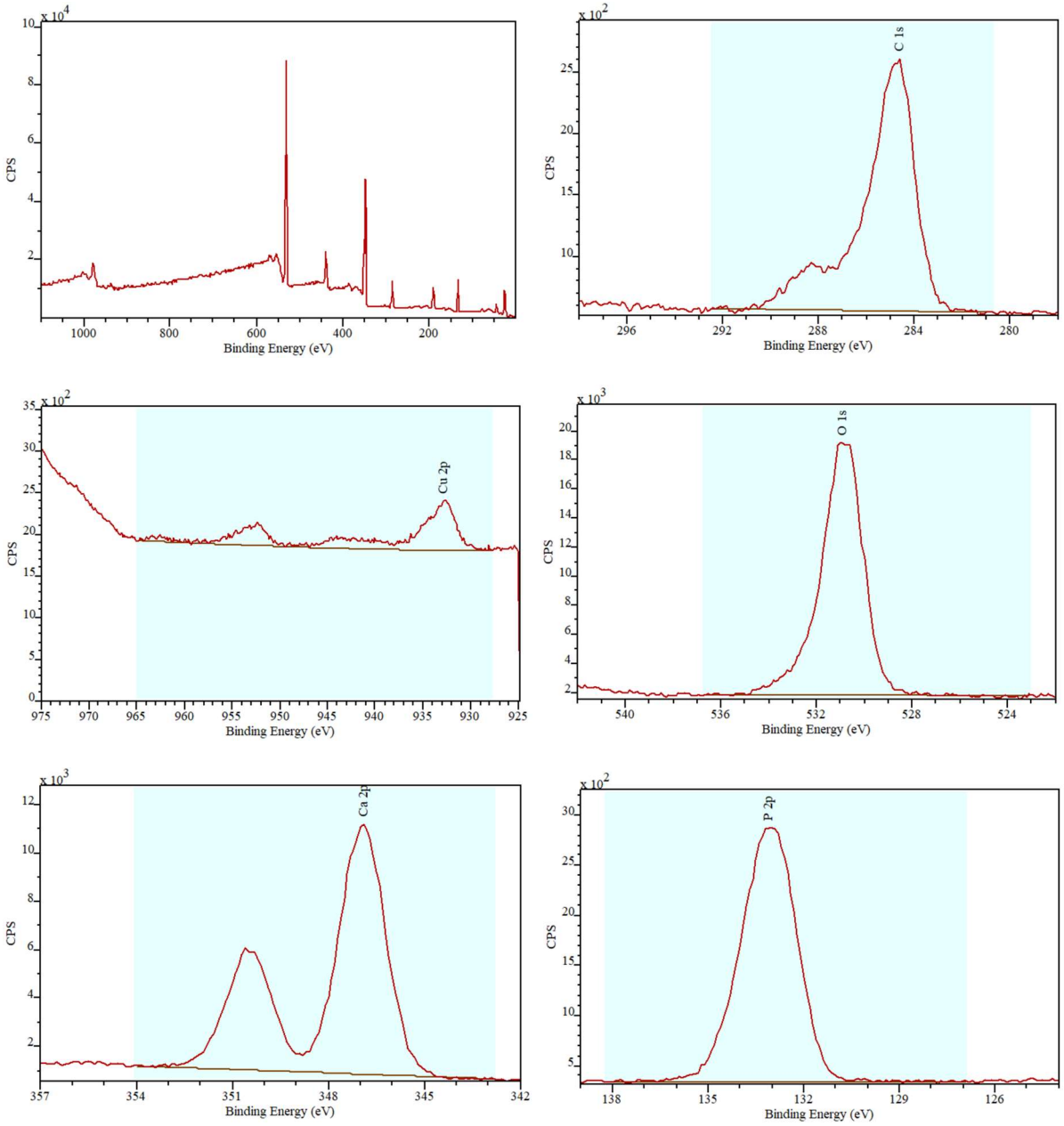

Figure S13. XPS spectra of the Cu-HAp(A) 450-12 sample.

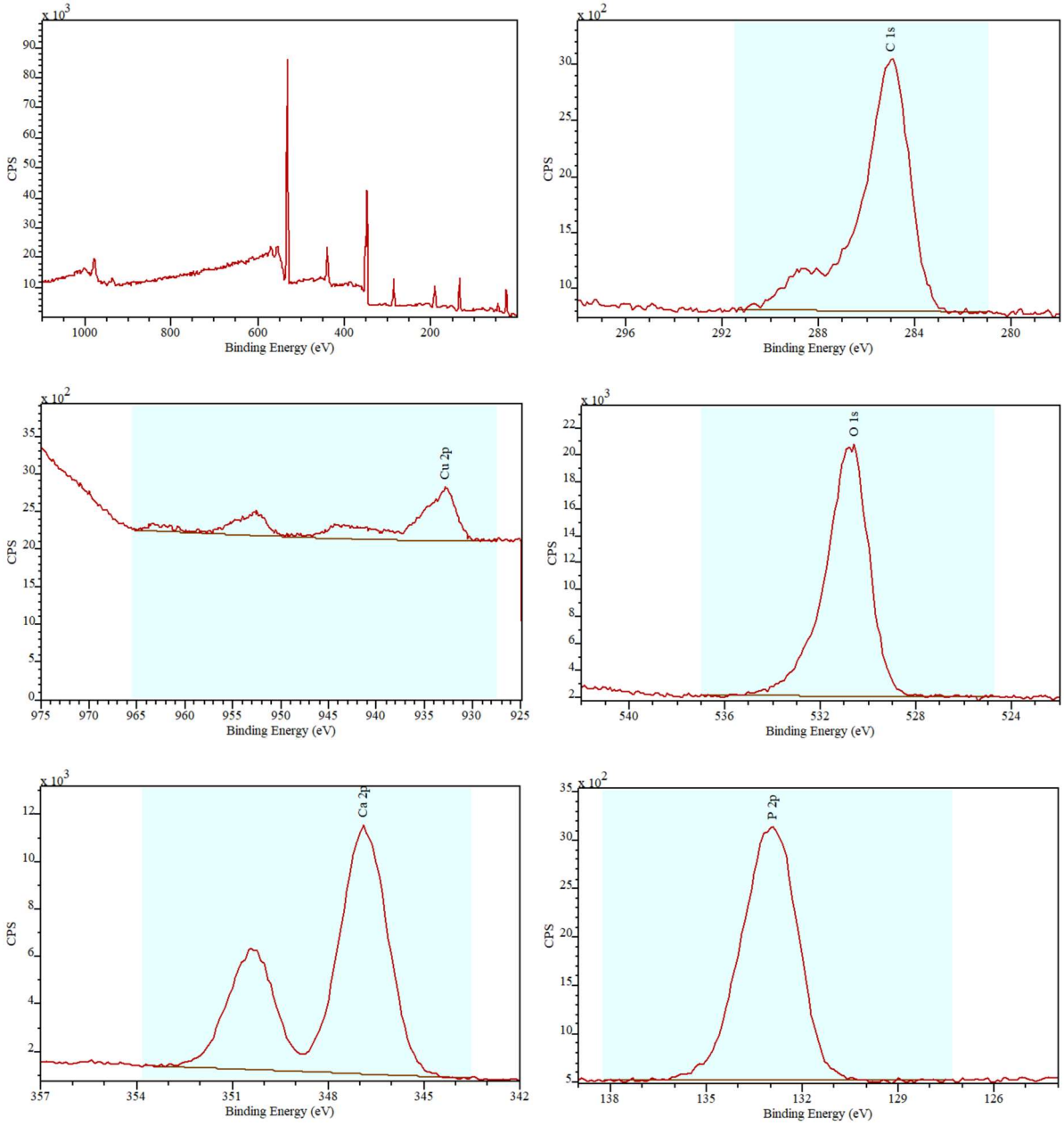

Figure S14. XPS spectra of the Cu-HAp(B) 600-12 sample.

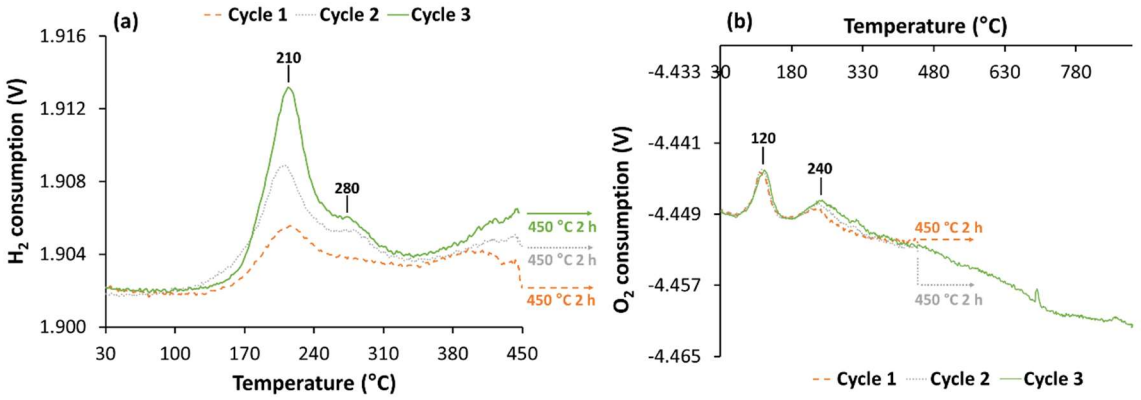

Figure S15. H_2 consumption (a) and O_2 consumption (b) profiles in three successive cycles of temperature programmed reduction (TPR, a) – temperature programmed oxidation (TPO, b) on the same Cu-HAp(A) sample. The sample (100 mg) was beforehand treated *ex situ* under Ar (100 mL/min) at 500 °C (5 °C/min from room temperature) for 1.5 h, and then *in situ* under O_2(5%)/He (25 mL/min) at 500 °C (10 °C/min from room temperature) for 1 h. TPR and TPO experiments were then alternately performed under H_2(5%)/He (25 mL/min) and O_2(5%)/He (25 mL/min), respectively. Each TPR experiment was immediately followed by a TPO one before the next TPR experiment was performed. In each TPR/TPO experiment, the sample was heated from room temperature to 450 °C at 10 °C/min, and then left under the reduction or oxidation flow for another 2 h, except in the last TPO experiment. The latter consisted of heating the sample up to 900 °C (10 °C/min) without stop at 450 °C.

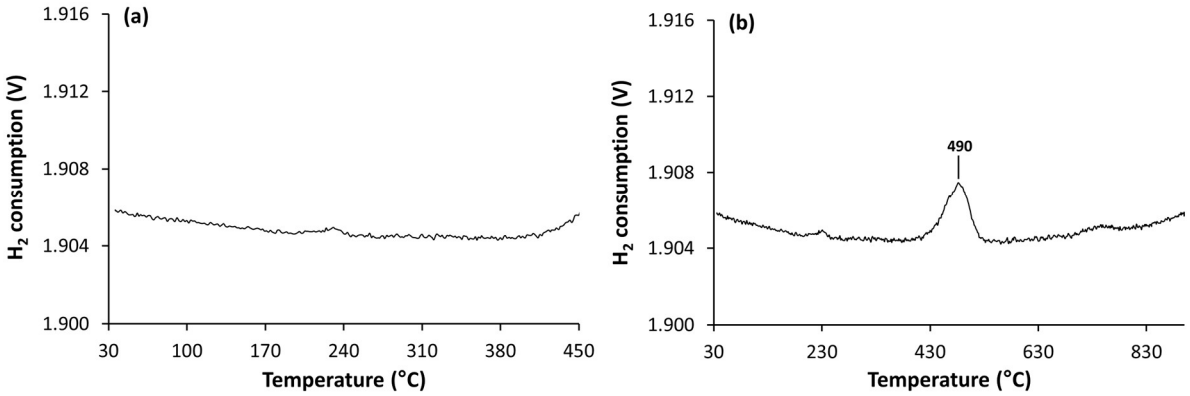

Figure S16. H_2 consumption profile in the TPR experiment performed on non-Cu-substituted HAp. In (a), the profile is shown only in the temperature range in which the TPR experiments on the Cu-HAp samples were performed (30 to 450 °C), for direct comparison with Figure S6a. In (b), the profile is shown up to 900 °C. The sample (100 mg) was beforehand treated *ex situ* under Ar (100 mL/min) at 500 °C (5 °C/min from room temperature) for 1.5 h, and then *in situ* under O_2(5%)/He (25 mL/min) at 500 °C (10 °C/min from room temperature) for 1 h. The TPR was performed under H_2(5%)/He (25 mL/min) at 10 °C/min.

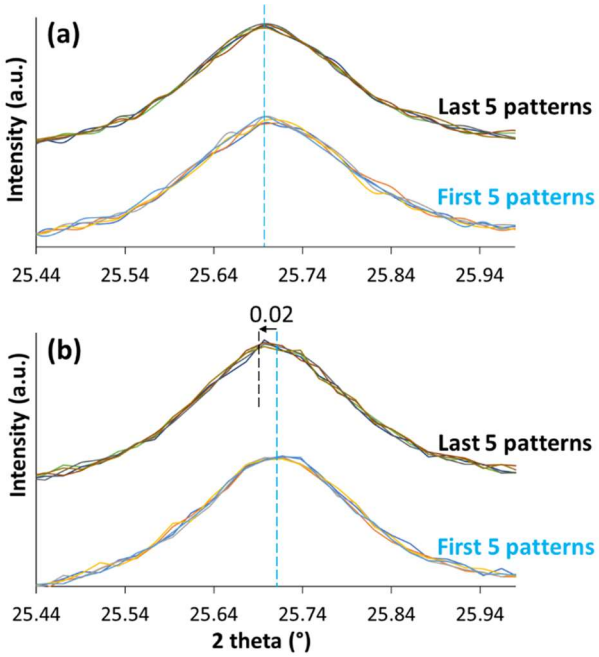

Figure S17. *In situ* XRD patterns of the Cu-HAp(A) sample at 450 °C, first overnight under He (30 mL/min) (a) and finally under H_2(10%)/Ar (30 mL/min) for 12 h (b), in the region of the (002) diffraction line. The sample - beforehand treated under Ar (100 mL/min) at 500 °C (5 °C/min from room temperature) for 1.5 h - was heated from room temperature to 500 °C under He (30 mL/min), at 3 °C/min with 45 min-stops every 50 °C. The sample was then cooled to 450 °C, and first kept overnight under He (30 mL/min) before being finally exposed to a flow of H_2(10%)/Ar. In both (a) and (b), the XRD patterns were measured successively during the first 2.5 h (first 5 patterns at the bottom) and the last 2.5 h (last 5 patterns at the top) under He and H_2(10%)/Ar, respectively. Each pattern was measured from 20 to 55 °, with a step size of 0.02 ° and a time/step of 1 s (28.3 min/pattern).

The slight shift to higher angles of the first 5 patterns under H_2(10%)/Ar (Figure S8b) as compared to the last 5 patterns under He (Figure S8a) is attributed to a slight change of sample height induced by suddenly replacing the flow of He by that of H_2(10%)/Ar.

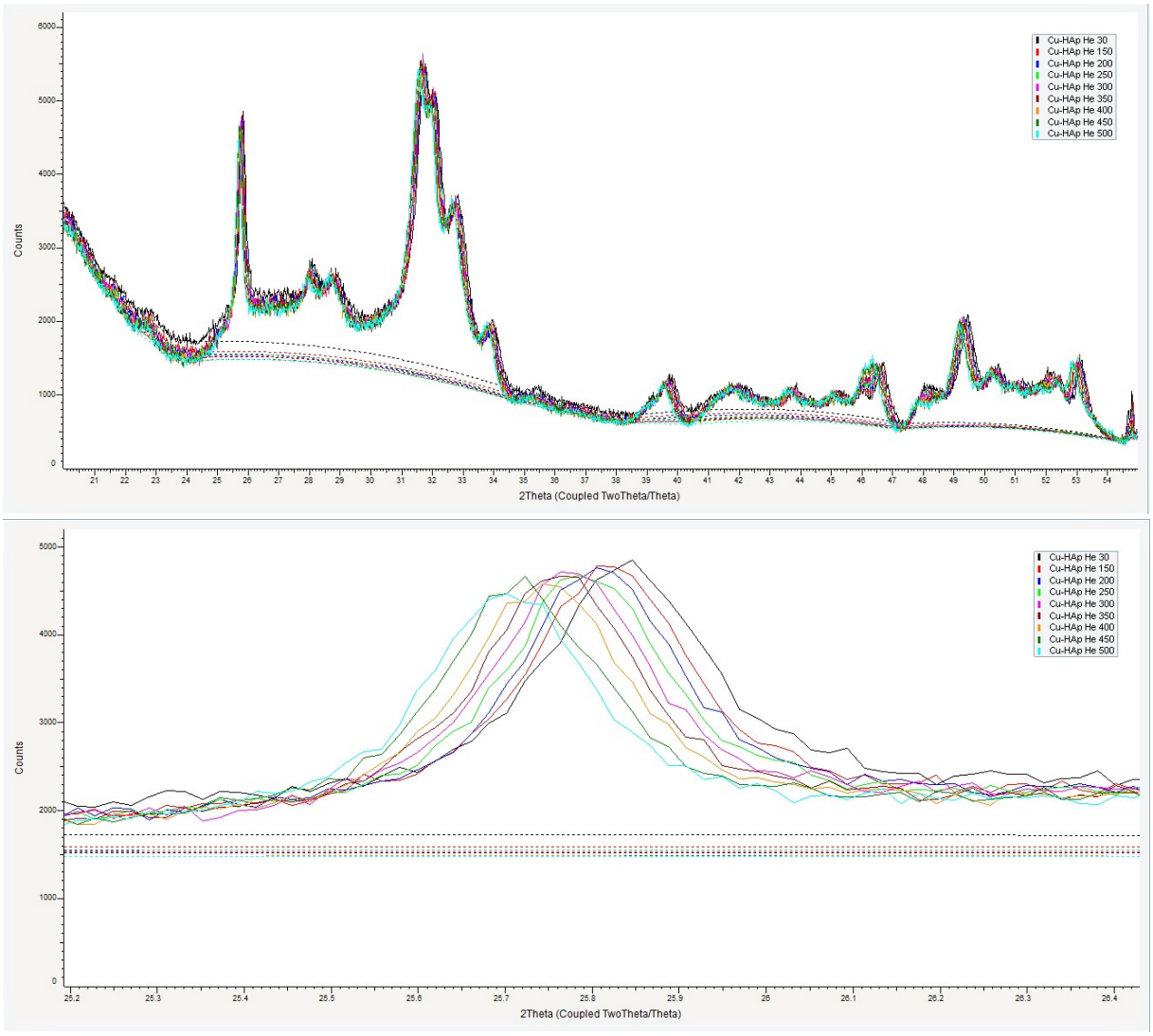

Figure S18. *In situ* XRD patterns of the Cu-HAp(A) sample under He (30 mL/min) from 30 to 500 °C (3 °C/min, with 45 min-stops every 50 °C), in the 2 theta range from 20 to 55 ° (top) and in the 2 theta range of the (002) diffraction line (bottom). The sample had beforehand been treated under Ar (100 mL/min) at 500 °C (5 °C/min from room temperature) for 1.5 h. Each XRD pattern was measured from 20 to 55 °, with a step size of 0.02 ° and a time/step of 1 s (28.3 min/pattern).

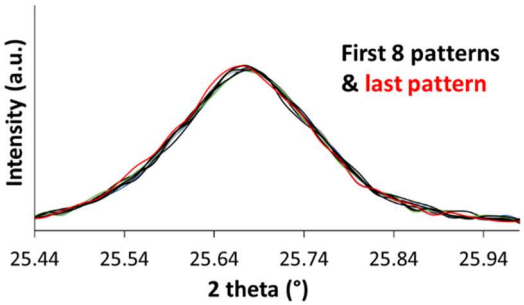

Figure S19. *In situ* XRD patterns of a non-Cu-substituted HAp sample at 450 °C under H_2(10%)/Ar (30 mL/min) for 12 h, in the region of the (002) diffraction line. The sample was prepared and pre-treated in the same conditions as the Cu-HAp(A) sample. In the *in situ* XRD experiment, it was heated from room temperature to 500 °C under He (30 mL/min), at 3 °C/min with 45 min-stops every 50 °C. It was then cooled to 450 °C, before being finally exposed to the flow of H_2(10%)/Ar. The XRD patterns were measured successively during the first 4 h (first 8 patterns at the bottom) and the last 30 min (last pattern at the top). Each pattern was measured from 20 to 55 °, with a step size of 0.02 ° and a time/step of 1 s (28.3 min/pattern).

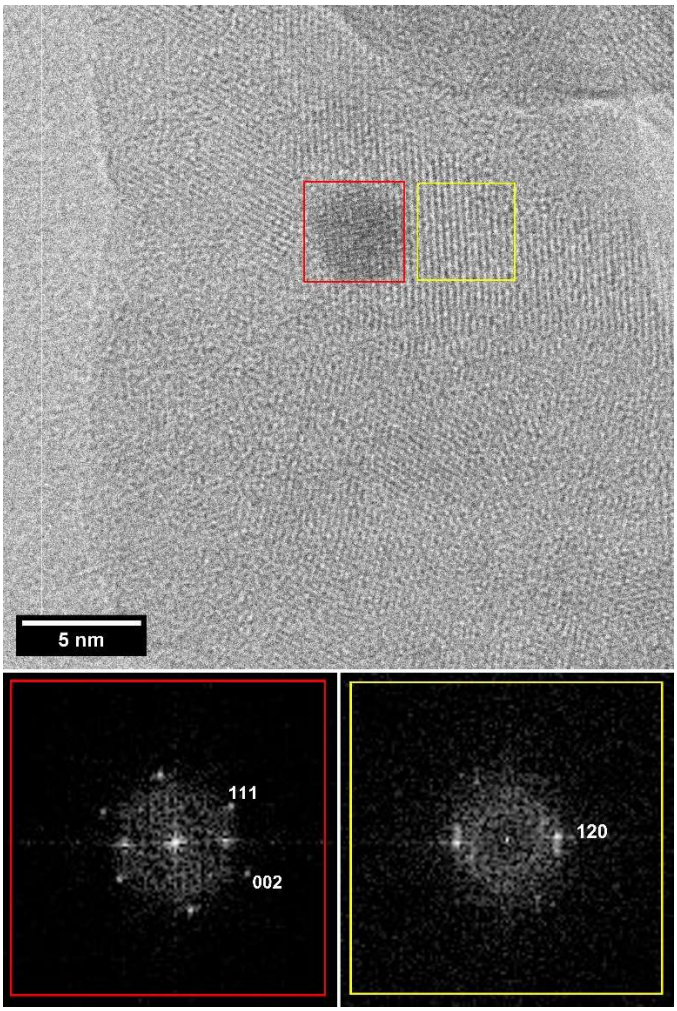

Figure S20. Top: HR-TEM image of the Cu-HAp(B) 600-12 sample; Bottom: fast Fourier transform (FFT) of the red and yellow squared areas within the top image.

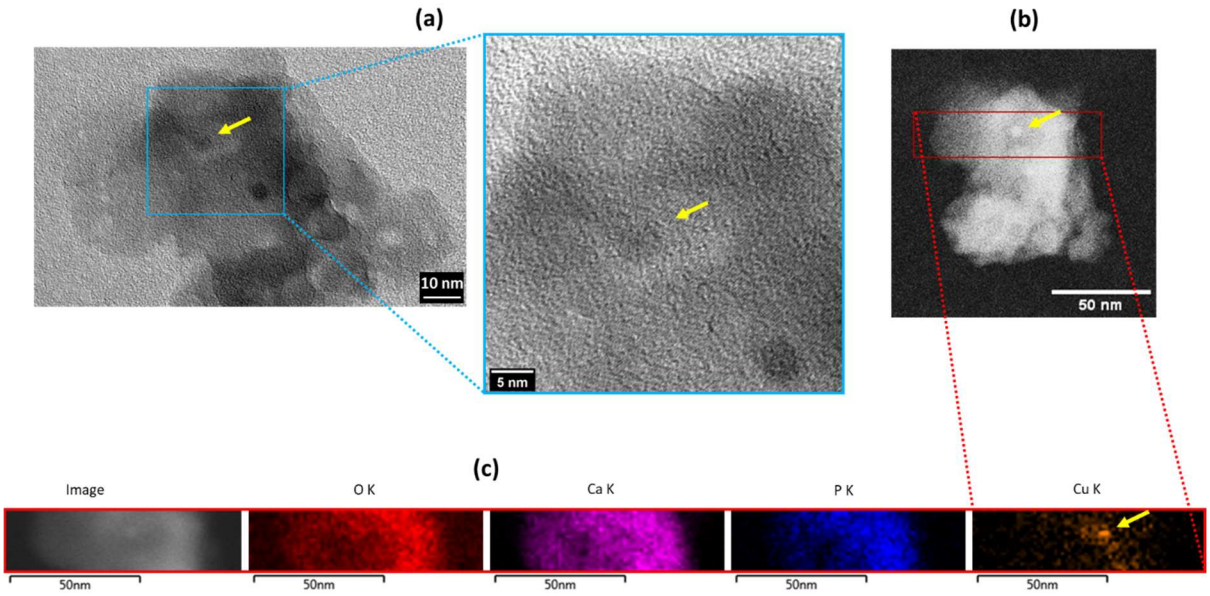

Figure S21. HR-TEM (a) and STEM-HAADF (b) images of the Cu-HAp 600-12 sample, with (c) corresponding STEM-EDX maps. The sample was beforehand treated first under Ar (100 mL/min) at 500 °C (5 °C/min from room temperature) for 1.5 h, and later under H_2(20%)/He (50 mL/min) at 600 °C for 12 h. In the latter treatment, the sample was heated from room temperature to 600 °C at 10 °C/min already under the H_2(20%)/He flow.

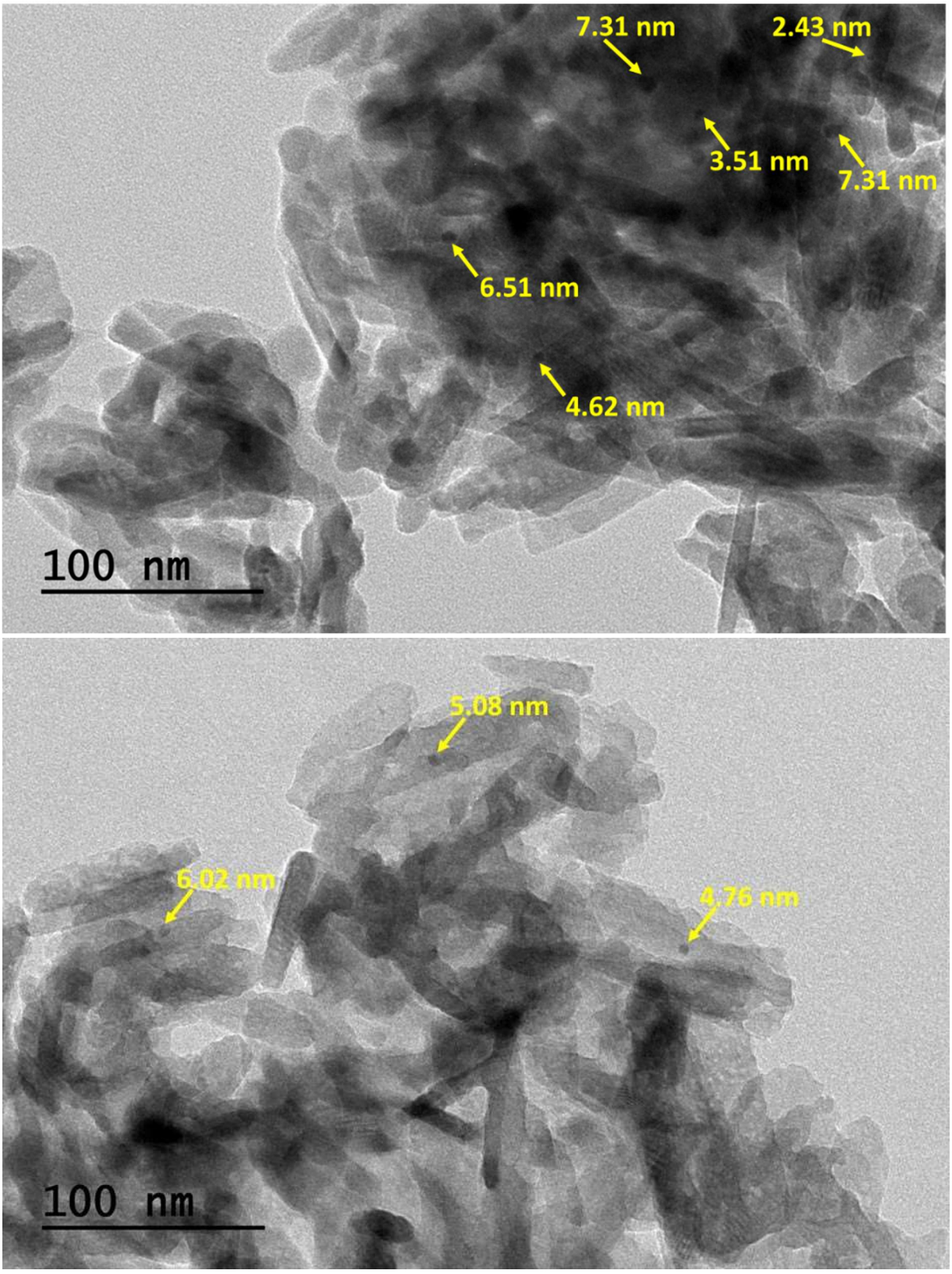

Figure S22. HR-TEM images of the Cu-HAp 600-12 sample. Indicated sizes (nm) correspond to the diameter of the arrow-pointed Cu particles. The sample was beforehand treated first under Ar (100 mL/min) at 500 °C (5 °C/min from room temperature) for 1.5 h, and later under H_2(20%)/He (50 mL/min) at 600 °C for 12 h. In the latter treatment, the sample was heated from room temperature to 600 °C at 10 °C/min already under the H_2(20%)/He flow.

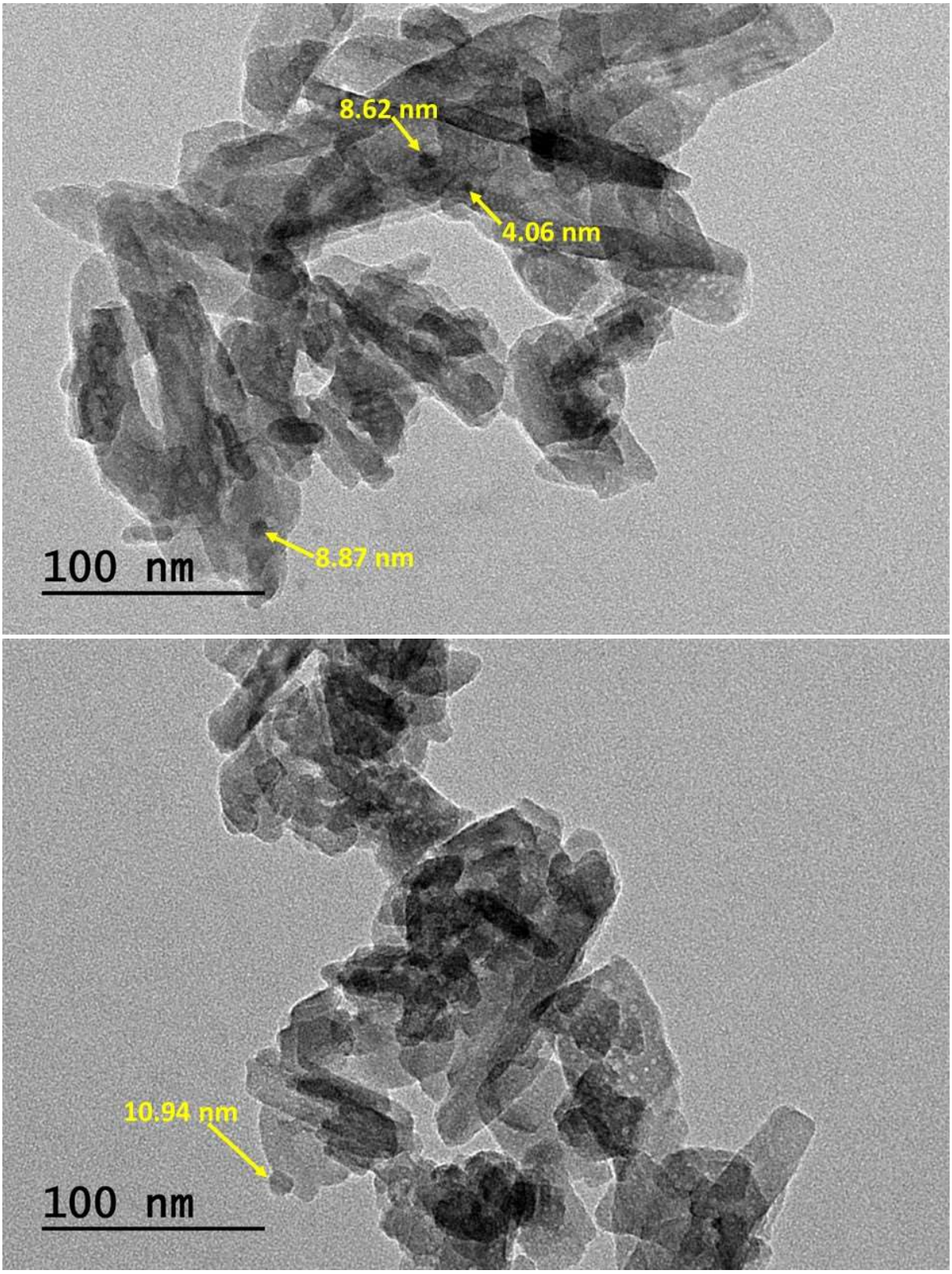

Figure S23. HR-TEM images of the Cu-HAp 600-12 sample. Indicated sizes (nm) correspond to the diameter of the arrow-pointed Cu particles. The sample was beforehand treated first under Ar (100 mL/min) at 500 °C (5 °C/min from room temperature) for 1.5 h, and later under H_2(20%)/He (50 mL/min) at 600 °C for 12 h. In the latter treatment, the sample was heated from room temperature to 600 °C at 10 °C/min already under the H_2(20%)/He flow.